



Defense Threat Reduction Agency
8725 John J. Kingman Road, MS
6201 Fort Belvoir, VA 22060-6201



DTRA-TR-16-77

TECHNICAL REPORT

Computational Characterization of Impact Induced Multi-Scale Dissipation in Reactive Solid Composites

Distribution Statement A. Approved for public release; distribution is unlimited.

July 2016

HDTRA1-10-1-0018

Keith A. Gonthier

Prepared by:
Louisiana State University
Baton Rouge, LA 70803

DESTRUCTION NOTICE:

Destroy this report when it is no longer needed.
Do not return to sender.

PLEASE NOTIFY THE DEFENSE THREAT REDUCTION
AGENCY, ATTN: DTRIAC/ J9STT, 8725 JOHN J. KINGMAN ROAD,
MS-6201, FT BELVOIR, VA 22060-6201, IF YOUR ADDRESS
IS INCORRECT, IF YOU WISH IT DELETED FROM THE
DISTRIBUTION LIST, OR IF THE ADDRESSEE IS NO
LONGER EMPLOYED BY YOUR ORGANIZATION.

REPORT DOCUMENTATION PAGE

Form Approved
OMB No. 0704-0188

The public reporting burden for this collection of information is estimated to average 1 hour per response, including the time for reviewing instructions, searching existing data sources, gathering and maintaining the data needed, and completing and reviewing the collection of information. Send comments regarding this burden estimate or any other aspect of this collection of information, including suggestions for reducing the burden, to Department of Defense, Washington Headquarters Services, Directorate for Information Operations and Reports (0704-0188), 1215 Jefferson Davis Highway, Suite 1204, Arlington, VA 22202-4302. Respondents should be aware that notwithstanding any other provision of law, no person shall be subject to any penalty for failing to comply with a collection of information if it does not display a currently valid OMB control number.

PLEASE DO NOT RETURN YOUR FORM TO THE ABOVE ADDRESS.

1. REPORT DATE (DD-MM-YYYY) 00-07-2016			2. REPORT TYPE Final Report		3. DATES COVERED (From - To) March 2010-August 2015	
4. TITLE AND SUBTITLE Computational Characterization of Impact Induced Multi-Scale Dissipation in Reactive Solid Composites					5a. CONTRACT NUMBER HDTRA1-10-1-0018	
					5b. GRANT NUMBER	
					5c. PROGRAM ELEMENT NUMBER	
6. AUTHOR(S) Gonthier, Keith, A					5d. PROJECT NUMBER	
					5e. TASK NUMBER	
					5f. WORK UNIT NUMBER	
7. PERFORMING ORGANIZATION NAME(S) AND ADDRESS(ES) Louisiana State University Baton Rouge, Louisiana, 70803					8. PERFORMING ORGANIZATION REPORT NUMBER	
9. SPONSORING/MONITORING AGENCY NAME(S) AND ADDRESS(ES) Defense Threat Reduction Agency 8725 John J. Kingman Road Fort Belvoir, VA 22060-6201					10. SPONSOR/MONITOR'S ACRONYM(S) DTRA	
					11. SPONSOR/MONITOR'S REPORT NUMBER(S) DTRA-TR-16-77	
12. DISTRIBUTION/AVAILABILITY STATEMENT Distribution Statement A. Approved for public release; distribution is unlimited.						
13. SUPPLEMENTARY NOTES						
14. ABSTRACT Mesoscale and macroscale modeling and simulation (M&S) were used to characterize shock induced dissipation in low density granular explosives (HMX, and HMX-AI composites). Emphasis was placed on characterizing how material microstructure (particle size and packing density) and composition (metal mass fraction) affect shock heating of the explosive component which establishes shock sensitivity and survivability. Predicted variations in hot-spot formation rate with shock strength were used to develop a microstructure-dependent ignition and burn model for low density HMX. The model was used to computationally examine initiation mechanisms resulting from low pressure shock input.						
15. SUBJECT TERMS Low Density HMX, Porous HMX, Meso-Scale Modeling and Simulation, Hot-Spot Formation, Shock Initiation, Deflagration to Detonation Transition, Ignition and Burn Modeling						
16. SECURITY CLASSIFICATION OF:			17. LIMITATION OF ABSTRACT	18. NUMBER OF PAGES	19a. NAME OF RESPONSIBLE PERSON	
a. REPORT	b. ABSTRACT	c. THIS PAGE			Allen Dalton	
U	U	U	SAR	50	19b. TELEPHONE NUMBER (Include area code) 703-767-4663	

UNIT CONVERSION TABLE

U.S. customary units to and from international units of measurement^{*}

U.S. Customary Units	<div style="display: flex; align-items: center; justify-content: center;"> <div style="margin-right: 10px;"> </div> Multiply by </div> <div style="display: flex; align-items: center; justify-content: center;"> <div style="margin-right: 10px;"> </div> Divide by[†] </div>	International Units
Length/Area/Volume		
inch (in)	2.54 × 10 ⁻²	meter (m)
foot (ft)	3.048 × 10 ⁻¹	meter (m)
yard (yd)	9.144 × 10 ⁻¹	meter (m)
mile (mi, international)	1.609 344 × 10 ³	meter (m)
mile (nmi, nautical, U.S.)	1.852 × 10 ³	meter (m)
barn (b)	1 × 10 ⁻²⁸	square meter (m ²)
gallon (gal, U.S. liquid)	3.785 412 × 10 ⁻³	cubic meter (m ³)
cubic foot (ft ³)	2.831 685 × 10 ⁻²	cubic meter (m ³)
Mass/Density		
pound (lb)	4.535 924 × 10 ⁻¹	kilogram (kg)
unified atomic mass unit (amu)	1.660 539 × 10 ⁻²⁷	kilogram (kg)
pound-mass per cubic foot (lb ft ⁻³)	1.601 846 × 10 ¹	kilogram per cubic meter (kg m ⁻³)
pound-force (lbf avoirdupois)	4.448 222	newton (N)
Energy/Work/Power		
electron volt (eV)	1.602 177 × 10 ⁻¹⁹	joule (J)
erg	1 × 10 ⁻⁷	joule (J)
kiloton (kt) (TNT equivalent)	4.184 × 10 ¹²	joule (J)
British thermal unit (Btu) (thermochemical)	1.054 350 × 10 ³	joule (J)
foot-pound-force (ft lbf)	1.355 818	joule (J)
calorie (cal) (thermochemical)	4.184	joule (J)
Pressure		
atmosphere (atm)	1.013 250 × 10 ⁵	pascal (Pa)
pound force per square inch (psi)	6.984 757 × 10 ³	pascal (Pa)
Temperature		
degree Fahrenheit (°F)	[T(°F) - 32]/1.8	degree Celsius (°C)
degree Fahrenheit (°F)	[T(°F) + 459.67]/1.8	kelvin (K)
Radiation		
curie (Ci) [activity of radionuclides]	3.7 × 10 ¹⁰	per second (s ⁻¹) [becquerel (Bq)]
roentgen (R) [air exposure]	2.579 760 × 10 ⁻⁴	coulomb per kilogram (C kg ⁻¹)
rad [absorbed dose]	1 × 10 ⁻²	joule per kilogram (J kg ⁻¹) [gray (Gy)]
rem [equivalent and effective dose]	1 × 10 ⁻²	joule per kilogram (J kg ⁻¹) [sievert (Sv)]

^{*} Specific details regarding the implementation of SI units may be viewed at <http://www.bipm.org/en/si/>.

[†] Multiply the U.S. customary unit by the factor to get the international unit. Divide the international unit by the factor to get the U.S. customary unit.

FINAL REPORT

Defense Threat Reduction Agency

Computational Characterization of Impact Induced Multi-Scale Dissipation in Reactive Solid Composites

Principal Investigator: Keith A. Gonthier
Mechanical and Industrial Engineering Department
Louisiana State University
Baton Rouge, Louisiana 70803
Email: *gonthier@me.lsu.edu*

Award Number: HDTRA1-10-1-0018
Performance Period: March 2010-August 2015

February 24, 2016

Contents

1	Abstract	4
2	Shock Dissipation in Low Density Granular Explosives	5
2.1	Significance	5
2.2	Goals and Methods	5
2.3	Work Accomplished	7
3	Analysis of Hot-Spots in Low Density Granular Explosives	14
3.1	Significance	14
3.2	Goals and Methods	15
3.3	Work Accomplished	15
4	Ignition and Burn Modeling for Low Density HMX	28
4.1	Significance	28
4.2	Goals and Methods	28
4.3	Work Accomplished	28
5	Personnel Supported	39
6	Publications and Conference Presentations	40
7	Workshop and Meeting Presentations	42
8	Manuscripts in Review/Preparation	42
9	Abstracts Accepted for Presentation	42

List of Figures

1	Initial microstructure for an ensemble of explosive and metal particles having $\lambda_m = 0.2$ and $\phi_{s0} = 0.835$. Explosive particles are colored red and metal particles are colored blue.	7
2	Predicted variation in Hugoniot curves with λ_m ($\phi_{s0} = 0.835$): (a) U_p - D plane; (b) U_p - \bar{P} plane; and (c) U_p - ϕ plane.	8
3	Predictions for effective component-specific spatial profiles within a (a) <i>strength dominated</i> shock ($U_p = 100$ m/s) and (b) <i>pressure</i> dominated shock ($U_p = 500$ m/s). The metal mass fraction is $\lambda_m = 0.20$. The effective phase-specific pressure and Von-Mises stress is shown in each case. Standard deviations about the effective profiles are shown as thin dashed curves. Black curves correspond to neat HMX.	10
4	Predictions for hot-spot mass fraction curves within a (a) <i>strength dominated</i> shock ($U_p = 100$ m/s) and (b) <i>pressure</i> dominated shock ($U_p = 500$ m/s). The metal mass fraction is $\lambda_m = 0.20$. The black curves are the effective dissipative heating rates of the (a) explosive and (b) metal components.	12
5	Illustration of the temperature thresholding technique used to identify hot-spots. Here, $T_{th} = 500$ K denotes the temperature threshold.	16
6	Representative initial particle ensembles used with mesoscale M&S to assess the effect of packing density on hot-spot formation in low density HMX.	17
7	Predicted variation in (a) hot-spot number density, (b) hot-spot volume fraction, and (c) hot-spot specific surface area for each ensemble with piston speed. The dashed lines represent best-fit exponential functions.	18
8	An illustration of hot-spot axial spacing used to compute the formation time between successive hot-spots based on their centroid locations.	19
9	Predicted variation in hot-spot formation time distribution with U_p for steady waves in porous HMX: (a) $\bar{\phi}_0 = 0.68$; (b) $\bar{\phi}_0 = 0.84$	20
10	Predicted variation in the effective hot-spot formation rate with (a) piston speed and (b) shock pressure for low density HMX.	21
11	(a) Predicted variation in the global ignition time with wave strength for porous HMX having different values of $\bar{\phi}_0$. (b) Comparison of the predicted ignition curve with initiation time data for $\bar{\phi}_0 = 0.68$	23
12	Initial particle ensembles with varying packing densities $\bar{\phi}_s$ and composition λ_m . Here, red particles represent Al, and yellow particles represent HMX.	24
13	Predicted variations in effective shock end states as function of $\bar{\phi}_s$ and λ_m : (a) \bar{P} - U_p ; (b) D - U_p ; (c) \bar{W}_{pe} - U_p ; and (d) \bar{W}_{pe} - \bar{P}	25
14	Predicted variations in the effective plastic work of the explosive component as a function of $\bar{\phi}_s$, and λ_m	26
15	Meso-structures with varying particle sizes, particle distributions and composition. Here, red particles represent metal, and yellow particles represent explosive.	26
16	Predicted variations in explosive dissipative work with particle size ratio and shock pressure for a granular HMX-Al composite having $\bar{\phi}_s = 0.84$: (a) $\lambda_m = 0.20$ and (b) $\lambda_m = 0.56$	27
17	Predicted variations in hot-spot volumetric properties with particle size ratio and shock pressure for a granular HMX-Al composite having $\bar{\phi}_s = 0.84$ and $\lambda_m = 0.20$: (a) number density and (b) volume fraction.	27

18	A comparison between mesoscale and continuum theory predictions for shock dissipation rate and dissipative work profiles corresponding to $U_p = 500$ m/s. Shock profiles are shown for different values of initial solid volume fraction $\bar{\phi}_0$. The shock is propagating from left to right in the figure.	31
19	A comparison between mesoscale and continuum theory predictions for (a) the variation in effective dissipative work with shock pressure and (b) the variation in compaction shock rise time with supporting piston speed.	31
20	A comparison of mesoscale M&S and continuum compaction theory predictions for dissipative work profiles induced by successive planar shock loading of low density HMX having $\phi_0 = 0.68$. The successive supporting piston speeds are $U_{P1} = 300$ m/s and $U_{P2} = 500$ m/s. (a) Mesoscale and (b) continuum theory spatial fields at various times. Fields are plotted in a right propagating piston-attached reference frame; the piston surface is located at $\xi = 0$ mm. (c) Mesoscale and (d) continuum theory predictions plotted in pressure-dissipated work phase space.	32
21	Plots showing the (a) ignition and initiation times, and (b) initiation distances for $\bar{\phi}_0 = 0.68$ and $\bar{\phi}_0 = 0.83$	36
22	Predicted (a) bulk/mixture pressure contours showing compaction shock and ignition front trajectories in the characteristic plane; (b) solid/explosive volume fraction contours in the characteristic plane; (c) variation in bulk pressure with position at various times; and (d) variation in dissipative compaction work with position at various times. The material is low density HMX ($\phi_0 = 0.68$) and the input shock corresponds to a supporting piston speed of $U_P = 200$ m/s. Position is shown in a piston-attached reference frame.	38

Computational Characterization of Impact Induced Multi-Scale Dissipation in Reactive Solid Composites

Keith A. Gonthier

Associate Professor

Mechanical and Industrial Engineering Department

Louisiana State University

Baton Rouge, Louisiana 70803

Phone: (225) 578-5915

FAX: (225) 578-5924

Email: *gonthier@me.lsu.edu*

1 Abstract

Reactive solid composites often consist of mixtures of high-explosive and metal particles (size ~ 0.001 - $200\ \mu\text{m}$), and polymeric binder. It remains fundamentally unclear, even for idealized systems, how microstructure (particle size, shape, and packing), component thermomechanical properties, and metal and binder mass fractions, affect impact induced heating of the explosive component which establishes their impact sensitivity and survivability.

This modeling and computational study had three key objectives: 1) To examine mesoscale dissipation by compaction shocks in low density granular/particulate explosives (HMX, and HMX-Al composites). For this objective, mesoscale modeling and simulation was performed using a technique that is well-suited for describing both volumetric and surface dissipation in granular systems that can induce thermally activated phenomena. The technique incorporates a thermoelastic-viscoplastic and stick-slip friction theory for each component to describe nonlinear deformation and motion, inter-particle friction, and plastic work. The relative importance of volumetric and surface dissipation within shock profiles was characterized, and its dependence on shock strength and metal mass fraction was examined. 2) To characterize how the microstructure and composition of low density granular explosives (HMX, and HMX-Al composites) affect shock induced formation of hot-spots. For this objective, inert temperature field predictions at the particle scale were combined with a thresholding strategy to identify hot-spot fields and to characterize their distributions in intensity, geometry, and spatial proximity in the deformed material configuration behind shocks. Such distributions are significant because they establish local ignition and control the rate of flame spread within the material. 3) To develop a thermodynamically compatible macroscale ignition and burn model that explicitly incorporates computationally derived relations between microstructure, shock strength, and hot-spots. The model was used to computationally examine how shock induced transition to detonation in low density HMX is affected by input shock strength and initial packing density.

This report briefly summarizes the significance, key goals and methods, and work accomplished for each objective of this study. Only brief discussions of key results are given; detailed expositions can be found in the cited articles.

2 Shock Dissipation in Low Density Granular Explosives

2.1 Significance

Mesoscale Modeling and Simulation (M&S) is a potentially useful tool to characterize shock induced dissipation within granular explosives that drives thermally activated phenomena responsible for ignition and flame spread. The utility of this approach is in its ability to resolve thermomechanical fields at the particle scale that are difficult to experimentally interrogate. Therefore, mesoscale M&S can principally provide information about the influence of microstructure on the material's shock behavior. This information can be potentially used to engineer microstructures for desired performance, and may also be used to guide development of microstructure-dependent continuum theories for shock induced ignition and burn of granular explosives.

2.2 Goals and Methods

The goal of this effort was *to computationally examine dissipation within and behind uniaxial compaction shocks in low density granular explosives (HMX, and HMX-Al composites)*. Mesoscale M&S was performed to identify how Al mass fraction affects the spatial structure of piston supported compaction shocks. An identical particle size distribution and packing arrangement was used for all simulations to isolate the effects of material composition (i.e., Al mass fraction) from those due to variations in microstructure and packing arrangement. This study represents a systematic extension of the work by Panchadhara and Gonthier [11] which strictly focused on compaction shocks in low density HMX to establish a benchmark for characterizing the effects of metal additives on shock behavior. Emphasis was placed in this effort on examining how the inclusion of Al affects explosive component heating and hot-spots relative to that of neat HMX. Here, neat material refers to one that consists of only a single component.

The physical problem was posed as a multi-particle contact problem for the evolution of thermomechanical fields within particles. The coupled initial boundary value problem (IBVP) for the displacement field \mathbf{u} and temperature field T within explosive and metal particles was locally described by evolution equations for linear momentum and thermal energy. All particles were initially stationary and unstressed. A hyperelastic, multiplicative, finite strain constitutive theory was used to model the stress-strain behavior of explosive and metal particles resulting from impact. A Perzyna type over-stress model, coupled with an associative flow rule and a Von-Mises type yield criterion, was used to describe the evolution of inelastic strain. The hyperelastic material behavior was formulated in terms of the Kirchhoff stress tensor $\boldsymbol{\tau} = \sum_{i=1}^3 (\tau_{ii}) \mathbf{n}_i \otimes \mathbf{n}_i$, where \mathbf{n}_i and τ_{ii} are its orthonormal eigenvectors and corresponding eigenvalues which were computed from a stored strain energy function Ψ by $\tau_{ii} = \partial\Psi/\partial\ln(\lambda_{e,i})$. Here, $\lambda_{e,i}$ are the eigenvalues of the elastic component of the deformation gradient $\mathbf{F} \equiv \mathbf{I} + \nabla_0 \mathbf{u}$, where $\nabla_0 \equiv \partial(\cdot)/\partial\mathbf{X}$ is the Lagrangian gradient operator. The Kirchhoff stress tensor is related to the Cauchy stress tensor by $\boldsymbol{\tau} = J\boldsymbol{\sigma}$, which can be decomposed into volumetric and deviatoric components: $\tau_{ii} = J p + \bar{\tau}_{ii}$, where the pressure is given by $p = \partial\Psi/\partial\ln(J)$, the stress deviator is given by $\bar{\tau}_{ii} = \partial\Psi/\partial\ln(\bar{\lambda}_{e,i})$, and $\bar{\lambda}_{e,i} = J^{-1/3}\lambda_{e,i}$. The Jacobian $J = \det(\mathbf{F})$ characterizes volumetric deformation.

The contact traction vector between particles was prescribed by $\mathbf{t}_c = t_N \mathbf{n} + \mathbf{t}_t$, where t_N is the local compressive normal traction on contact boundaries defined by $t_N = -\mathbf{n} \cdot \boldsymbol{\sigma} \mathbf{n}$ and \mathbf{n} is the unit outward normal vector. The frictional traction vector \mathbf{t}_t was estimated using Amontons-Coulomb law of dry friction for which particle stick or slip was possible depending on the system dynamics. A contact was assumed to stick if $\phi_t \equiv |\mathbf{t}_t| - \mu t_N \leq 0$, where μ is the limiting friction coefficient; if the contact was sliding, then the tangential traction was given by $|\mathbf{t}_t| = \mu t_N$. The local heat flux due to frictional heating was given by $q_f = \mathbf{t}_c \cdot \mathbf{v}_r$, where \mathbf{v}_r is the relative tangential velocity. The total heat flux was distributed between the contacting bodies according to $q_f^{(1)} = \omega q_f$ and $q_f^{(2)} = (1 - \omega)q_f$, where the partition function ω was given by

$$\omega = \left(1 + \sqrt{\frac{k_T^{(2)} c_v^{(2)} \rho^{(2)}}{k_T^{(1)} c_v^{(1)} \rho^{(1)}}} \right)^{-1}. \quad (1)$$

The notation superscript (1) and (2) represent properties associated with the two particles in contact which consisted of either two explosive particles, a metal particle and an explosive particle, or two metal particles. Thermal contact resistance between particles was ignored.

An additive form of the stored energy function was used to describe the behavior of HMX and Al:

$$\Psi = G \sum_{i=1}^3 [\ln(\bar{\lambda}_{e,i})]^2 + \frac{k}{2} [\ln(J)]^2 - \frac{3\alpha k}{J} (T - T_0) \ln(J) + \rho_0 c_v \left[(T - T_0) - T \ln\left(\frac{T}{T_0}\right) \right]. \quad (2)$$

Here, G is the shear modulus, k is the bulk modulus, α is the linear coefficient of thermal expansion, and T_0 is the ambient temperature of the initially stress free ensemble. The effective plastic strain rate was estimated using a Perzyna type overstress model $\dot{\epsilon}_p \equiv \langle d/\gamma \rangle$, where the overstress $d \equiv \tau_e - \tau_0$, γ is the plastic viscosity parameter, and $\langle \cdot \rangle$ are the Macaulay brackets. In this expression $\tau_e = \sqrt{\frac{3}{2} \bar{\boldsymbol{\tau}} : \bar{\boldsymbol{\tau}}}$ is the effective (or Von Mises) stress and τ_0 is the initial yield stress. Explicit relations for pressure and deviatoric stress are given by

$$p = \frac{1}{J} \left(k \ln(J) - 3k\alpha(T - T_0) \frac{(1 - \ln(J))}{J} \right), \quad \bar{\tau}_{ii} = 2G \ln(\bar{\lambda}_{e,i}). \quad (3)$$

Key differences exist in several material properties for HMX and Al that influenced the deformation response of the mixture. First, the characteristic acoustic impedance, given by $Z = \rho_0 C_l$, where ρ_0 and C_l are the ambient density and longitudinal sound speed, is appreciably higher for the metal than the explosive ($Z_{metal}/Z_{expl} \approx 2.3$). Because the acoustic pressure goes as $P \sim Zu$, where u is the longitudinal particle speed, the inclusion of metal increased the average (or effective) wave pressure over that of neat granular HMX for a given microstructure and impact speed. An increase in effective wave pressure generally facilitated the elimination of porosity and enhanced hot-spot formation within the explosive component, though the degree of enhancement was mitigated by the extent of inelastic metal deformation because of its low yield stress ($\tau_{0,metal}/\tau_{0,expl} \approx 0.67$). Second, the thermal conductivity of the metal is significantly higher than that of the explosive ($k_{T,metal}/k_{T,expl} \approx 474$) which affected the partitioning of frictionally dissipated energy at metal-explosive contact surfaces. Based on ambient material densities, Eq. (1) gives $\omega \approx 0.05$; thus, approximately 95% of frictionally dissipated energy at contacts was absorbed by the metal which, in part, suppressed explosive hot-spot formation. The extent of suppression was dependent on both metal mass fraction and microstructure.

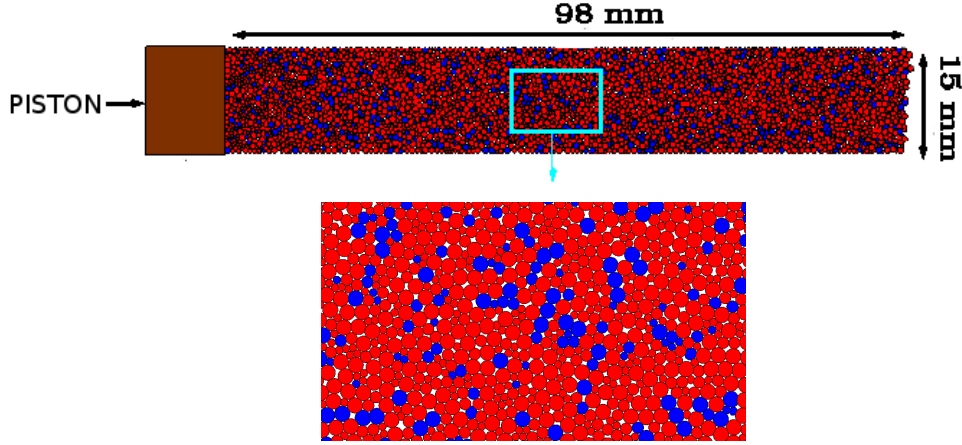


Figure 1: Initial microstructure for an ensemble of explosive and metal particles having $\lambda_m = 0.2$ and $\phi_{s0} = 0.835$. Explosive particles are colored red and metal particles are colored blue.

The computational technique used the finite-element method (FEM), coupled with a radial return stress update algorithm, to numerically integrate the time-dependent, 2-D conservation principles and viscoplastic flow rule governing deformation of individual particles, and used the discrete-element method (DEM) to account for interactions between particles. The DEM used a distributed, conservative potential based penalty method whereby the normal contact traction between particles was estimated by penalizing their penetration, and frictional tractions were estimated by a penalty regularized Amontons Coulomb law. Particles were discretized using constant strain, triangular (CST) finite elements. A temporally second-order accurate, explicit numerical technique was used to integrate the finite element equations for nodal displacements and temperatures. The constitutive theory was separately validated using Hugoniot data for granular HMX and porous Al.

2.3 Work Accomplished

Shock structures were computationally examined based on effective shock pressure relative to the material crush-up strength. Work accomplished as part of this effort along with key observations are briefly summarized below. Publications and presentations resulting from this work are indicated by the cited references.

1. **Analysis of computed Hugoniots.** [Chakravarthy, et. al., 2010; Chakravarthy and Gonthier, 2010; Gonthier, 2010; Chakravarthy and Gonthier, 2011; Chakravarthy, et al., 2013 A; Chakravarthy, 2014]. The deformation response of material having an initial solid volume fraction of $\phi_s^0 = 0.835$ (porosity $1 - \phi_s^0 = 0.165$) was characterized for different shock pressures and Al mass fractions. The microstructure consisted of initially circular, randomly packed HMX and Al particles having three discrete particle sizes of $d = (40, 50, 60) \mu\text{m}$, with a mean of $\bar{d} = 50 \mu\text{m}$, as illustrated in Fig. 1 for a particle ensemble having an Al mass fraction of $\lambda_m = 0.2$.

Figure 2 summarizes predicted Hugoniot curves for $\lambda_m = 0, 0.20, 0.56$, and 1 in the U_p - D and U_p - \bar{P} planes, respectively, where $\bar{P} = (\bar{P}_e\phi_e + \bar{P}_m\phi_m)/\phi_s$ is the effective equilibrium pressure behind the shock, $\phi_s = \phi_e + \phi_m$ is the total solid volume fraction behind the shock, and D

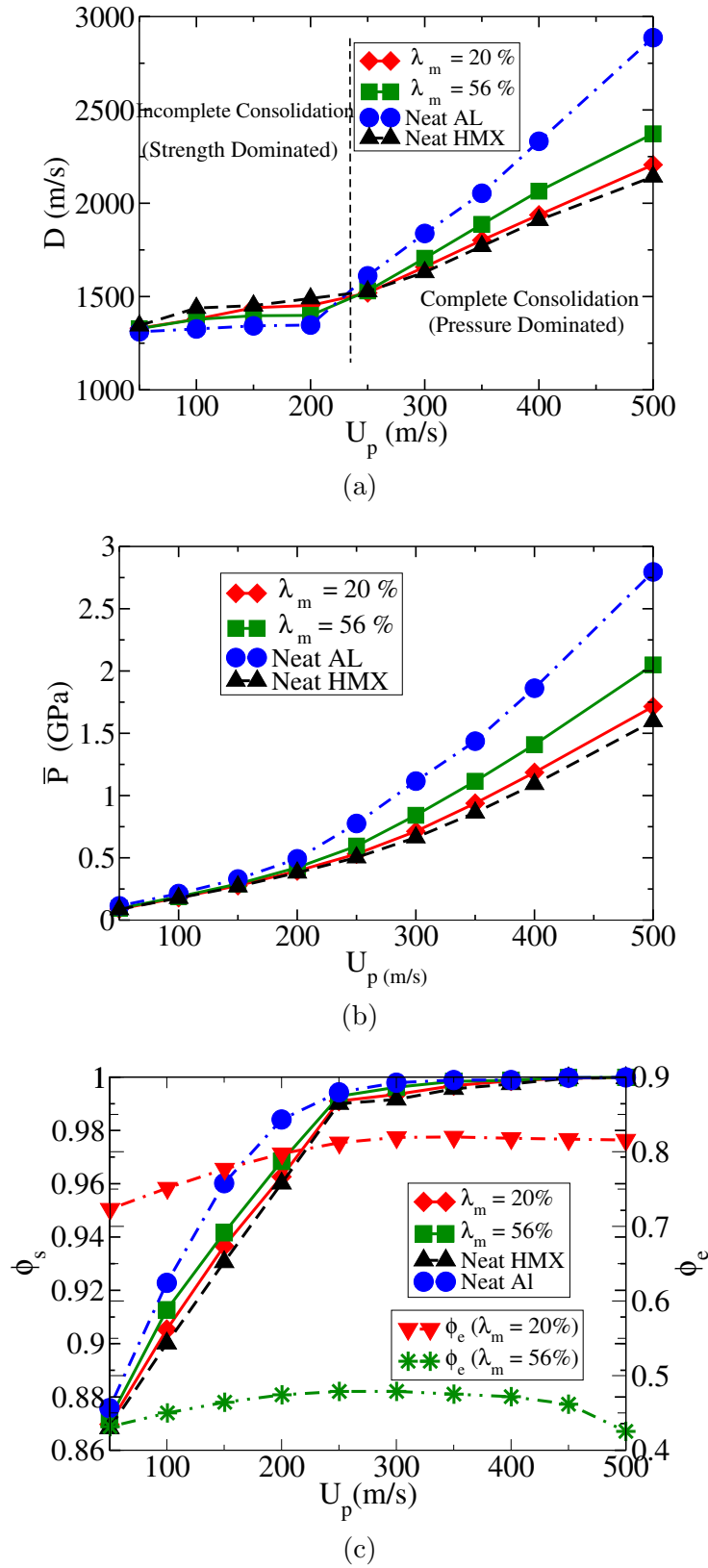


Figure 2: Predicted variation in Hugoniot curves with λ_m ($\phi_{s0} = 0.835$): (a) U_p - D plane; (b) U_p - \bar{P} plane; and (c) U_p - ϕ plane.

is the corresponding shock speed. Here, piston speeds within the range $50 \leq U_p \leq 500$ m/s were considered, where speeds of approximately $U_p \geq 250$ m/s resulted in nearly complete material crush-up and consolidation ($\phi_s \approx 1$) for all values of λ_m . This critical value of piston speed separates two well-defined wave categories: a low pressure category referred to as strength dominated because material strength is important in preventing complete pore collapse; and a high pressure category referred to as pressure dominated because the resulting pressure is sufficient to completely eliminate porosity. Material strength plays a less significant role than pressure for pressure dominated shocks.

A few observations are noteworthy. First, the effective shock pressure monotonically increases with λ_m for fixed U_p due to the high metal acoustic impedance which causes reflection of acoustic energy at explosive-metal interfaces thereby enhancing the deformation and pressure of explosive particles. This observation agrees with data for both neat granular HMX ($\lambda_m = 0$) and neat porous aluminum ($\lambda_m = 1$) [9]. Moreover, the inclusion of metal more significantly affects shock pressure for pressure dominated waves due to enhanced compression of consolidated material. Second, variations in D with λ_m qualitatively differ between the two wave categories. For strength dominated shocks, D slightly decreases with increasing λ_m whereas the opposite trend is predicted for pressure dominated shocks. Though speculative, this prediction is plausible because the lower metal yield strength can enhance dissipation by plastic work during pore collapse, even for neat granular metal ($\lambda_m = 1$), resulting in slightly lower wave speeds than those associated with neat granular HMX. However, dissipation by plastic flow becomes more geometrically constrained within shock profiles for pressure dominated shocks due to the elimination of porosity resulting in higher wave speeds. The weak variation in D with U_p for strength dominated shocks is largely due to inter-particle friction during pore collapse which enhances material rigidity. Simulations performed for frictionless contact indicate a larger decrease in D as $U_p \rightarrow 0$ for strength dominated waves (as illustrated Item 5 of this section). It is possible that particle fracture and rearrangement, and 3D effects, may cause a larger variation in D with U_p for strength dominated shocks by enhancing the mobility of fractured particles during crush-up.

Figure 2(c) gives the predicted variation in ϕ_s and ϕ_e behind the shock with U_p . These predictions illustrate that pressure dominated shocks result in nearly complete material consolidation for all values of λ_m . Moreover, mild variations in ϕ_e with U_p are predicted to occur following consolidation (with $\phi_m = 1 - \phi_e$), particularly for high pressure shocks, due to differences in component-specific compressibility. Because of the high metal bulk modulus ($K_{metal}/K_{expl} \approx 5.8$), the explosive is more easily compressed under high pressure confinement resulting in a slight reduction in its volume fraction. This effect is more pronounced for larger values of λ_m as shock pressure increases.

2. **The spatial structure of compaction shocks was computationally examined.** [Chakravarthy, et. al., 2010; Chakravarthy and Gonthier, 2010; Gonthier, 2010; Chakravarthy and Gonthier, 2011; Chakravarthy, et al., 2013 A; Chakravarthy, 2014] Figure 3 illustrates the predicted spatial variation in effective component pressure \bar{P}_i ($i = e, m$) and Von-Mises stress $\bar{\tau}_i$ for strength and pressure dominated shocks corresponding to $U_p = 100$ m/s and 500 m/s, respectively; the waves are propagating from left to right in the figure. Also shown for comparison are predicted profiles for neat HMX corresponding to the same piston speeds. Spatial variations in the standard deviation (σ) of the fluctuations are shown to highlight their local intensity about the effective states.

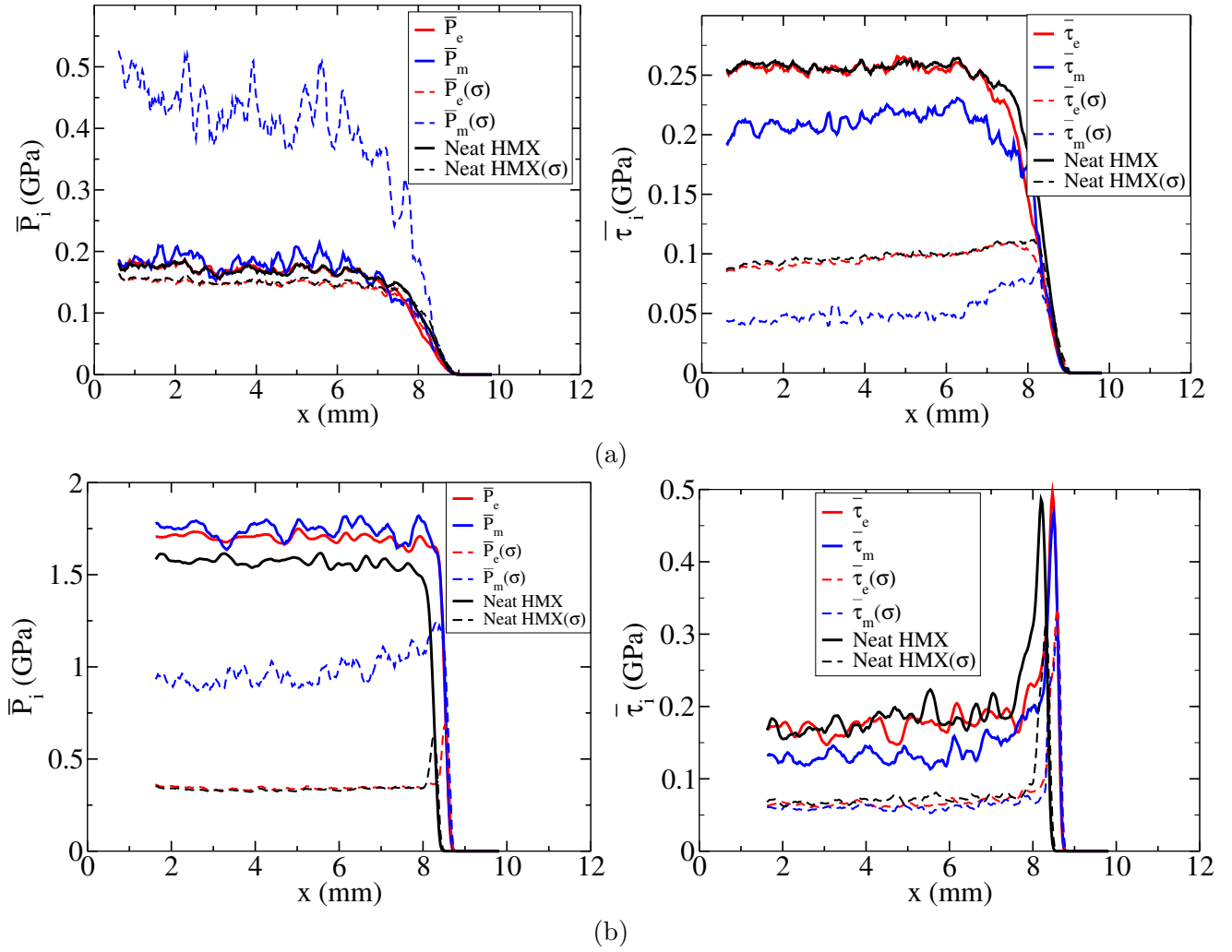


Figure 3: Predictions for effective component-specific spatial profiles within a (a) *strength dominated* shock ($U_p = 100$ m/s) and (b) *pressure dominated* shock ($U_p = 500$ m/s). The metal mass fraction is $\lambda_m = 0.20$. The effective phase-specific pressure and Von-Mises stress is shown in each case. Standard deviations about the effective profiles are shown as thin dashed curves. Black curves correspond to neat HMX.

The metal pressure within the strength dominated shock is marginally higher than that of the explosive, and the intensity of its fluctuations is considerably higher. Moreover, fluctuations in metal pressure appreciably exceed the effective value behind the shock [$\bar{P}_m(\sigma)/\bar{P}_m \approx 2.4$] which is indicative of high amplitude (relative to the effective pressure), high frequency acoustic ringing within the metal. The effective Von-Mises stress for the metal and explosive monotonically increase within the shock to values lower than their corresponding yield strength which is indicative of a small amount of inelastic deformation at the particle scale. The intensities of Von Mises stress fluctuations are low relative to their effective values. For approximately $\lambda_m \leq 0.3$, the compaction dynamics is dominated by explosive-explosive contact; therefore, only small differences between the explosive component and the neat HMX responses are predicted. Though not shown in the figure, the effective dissipative work within the metal is larger than that of the explosive due to its lower yield strength, and the in-

tensities of the fluctuations are high relative to their averages, particularly for the explosive component [$\overline{W}_{d,e}(\sigma)/\overline{W}_{d,e} \approx 2.5$] due to highly localized deformation.

Unlike the strength dominated shock, appreciably higher explosive component pressure is predicted behind the pressure dominated shock than for neat HMX due to stronger wave interactions occurring in the vicinity of explosive-metal contact surfaces. The high metal acoustic impedance causes the amplification of compression waves within explosive particles when reflected from metal interfaces resulting in a net increase in explosive pressure. Again, both the effective metal pressure and its fluctuations are higher than those of the explosive. Fluctuations in both explosive and metal pressure are appreciably lower than their effective values behind the shock [$\overline{P}_e(\sigma)/\overline{P}_e \approx 0.18$ and $\overline{P}_m(\sigma)/\overline{P}_m \approx 0.52$] indicating more spatially homogeneous fields, though substantial acoustic ringing still occurs within metal particles. The effective explosive and metal Von-Mises stresses overshoot their respective yield surfaces ($\tau_{o,e} = 0.37$ GPa, $\tau_{o,m} = 0.25$ GPa) before relaxing to quasi-steady values behind the shock. The Von-Mises stresses are sufficiently large to cause complete material consolidation, where compaction of explosive particles is primarily responsible for the reduction in porosity because the mass fraction of metal is low. The explosive dissipative work is comparable to that of the metal in this case, and is larger than that of neat explosive due to pressure enhanced compaction.

3. **Hot-spot mass fraction curves within and behind compaction shocks were computationally analyzed.** [Chakravarthy, et. al., 2010; Chakravarthy and Gonthier, 2010; Gonthier, 2010; Chakravarthy and Gonthier, 2011; Chakravarthy, et al., 2013 A] Considerable attention was placed in this effort on characterizing shock profiles in terms of compaction induced dissipation rate because it is believed to be a key macroscale hot-spot formation mechanism. Whether the dissipation rate is locally sufficient to overcome conductive cooling and promptly ignite the material for a given problem depends, in part, on its intensity and shock rise time. Therefore, it was instructive to characterize the spatial and temporal variation in integrated hot-spot mass within and behind compaction shocks; the resulting profiles are referred to as hot-spot mass fraction curves.

Figure 4 illustrates the spatial and temporal evolution of explosive component hot-spot mass fraction for the strength and pressure dominated shocks discussed above. Color bars in these plots represent the logarithm of mass-fraction (i.e., $\log m_i$) which better highlights the small amounts of mass that are locally heated to elevated temperature. Also shown in these plots is the effective component-specific dissipative heating rate to indicate the location and width of the shock. The fraction of heated mass steadily increases with distance behind the shock until a quasi-steady distribution is attained near the end of the shock deformation zone. The structure of explosive hot-spot mass fraction curves generally consists of three parts based on temperature rise. The first part includes mass-fractions within the range $10^{-1} \leq m_e \leq 10^{-3}$ that experience a temperature rise of $\Delta T \leq \Delta T_b \approx 100$ K; this heated mass is almost exclusively due to volumetric dissipation by plastic work. The second part of the distribution includes mass-fractions within the range $10^{-3} \leq m_e \leq 10^{-4}$ that are heated through a temperature rise of $\Delta T_b \leq \Delta T \leq \Delta T_f \approx 200$ K; this heated mass is due to both volumetric and surface dissipation, and it is stochastically dependent on the microstructure. The third part (or tail) of the distribution includes mass-fractions of $m_e \approx 10^{-5}$ that experience $\Delta T \geq \Delta T_f$; this heated mass is mostly due to surface dissipation by friction work, and is close to the resolution limit of the computations determined by the

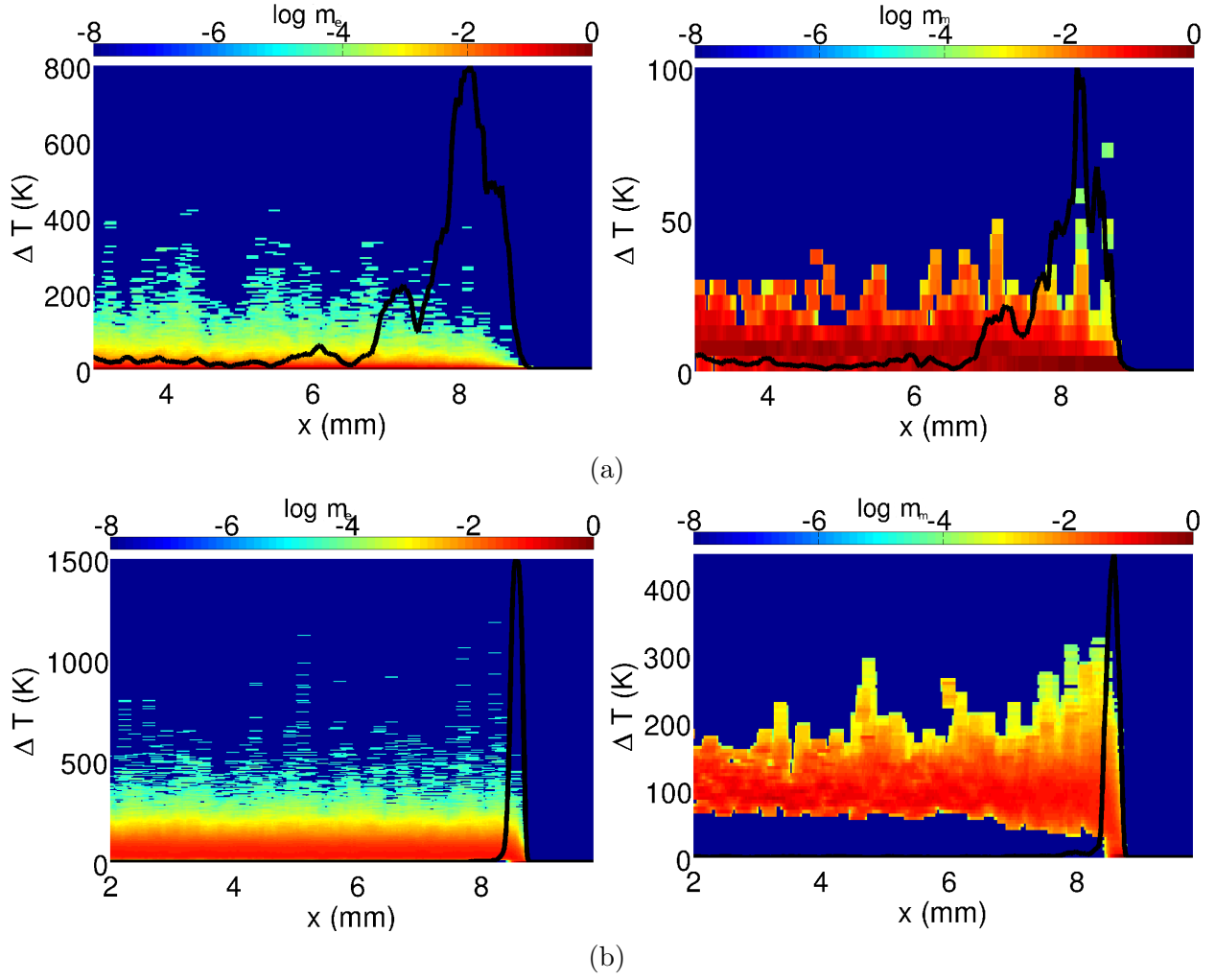


Figure 4: Predictions for hot-spot mass fraction curves within a (a) *strength dominated* shock ($U_p = 100$ m/s) and (b) *pressure dominated* shock ($U_p = 500$ m/s). The metal mass fraction is $\lambda_m = 0.20$. The black curves are the effective dissipative heating rates of the (a) explosive and (b) metal components.

mass of a single finite-element. The discrete appearance of the distribution tail is due to numerical discretization of the temperature field. For these computations, thermal diffusion lengths for HMX are smaller than the finite element size ($L_{element}/L_{diffusion} \approx 10$). Though thermal diffusion is included in the model, it has no discernible effect on the tail of the explosive component hot-spot curve; as such, explosive hot-spots are effectively adiabatic over simulation time-scales. The metal exhibits trends that are qualitatively similar to the explosive component with the exception that the high metal thermal diffusivity suppresses the formation of small, high frequency, frictionally induced hot-spots within the metal behind the shock. Unlike the explosive component, thermal conduction within the metal is resolved on the computational grid ($L_{element}/L_{diffusion} \approx 0.1$).

Shock thickness (and particle residence time within the shock) significantly decreases for pressure dominated shocks. As with strength dominated shocks, predicted hot-spot mass fraction

curves for the metal differ significantly from that of the explosive due to the absence of a frictionally induced high-temperature tail. Moreover, all metal mass experiences a temperature rise of at least $\Delta T_m \approx 80$ K and thermal diffusion causes a slight reduction in metal temperature with increasing distance behind the shock leading to more spatially homogeneous fields within particles. Again, only slight differences between the explosive component heating response and that of neat explosive are predicted because the fraction of metal mass is low. The temperature rises predicted here are sufficient to trigger local adiabatic ignition of small amounts of explosive mass, though it remains unclear whether a measurable global ignition event would subsequently result.

4. **The dependence of shock profiles on Al mass fraction was examined.** [Chakravarthy, et. al., 2010; Chakravarthy and Gonthier, 2010; Gonthier, 2010; Chakravarthy and Gonthier, 2011; Chakravarthy, et al., 2013 A; Chakravarthy, 2014] As mentioned, an increase in Al content increases the effective shock pressure of HMX-Al composites for a prescribed piston speed due to an increase in acoustic impedance of the composite. Though predicted pressure variations are qualitatively similar for strength and pressure dominated shocks, more appreciable increases in component pressures are predicted behind pressure dominated shocks as λ_m increases. However, contrary to strength dominated shocks, the effective plastic work in both the explosive and metal are predicted to increase with λ_m for pressure dominated shocks which is indicative of pressure enhanced compaction followed by compression of consolidated material.

Because the inclusion of metal enhances the effective explosive dissipative work by pressure dominated shocks, it increases explosive hot-spot mass. Moreover, an increase in λ_m causes a small increase in the fraction of explosive mass affected by plastic work and slightly suppresses the high temperature tail affected by friction work. The increase in heating by plastic work is consistent with pressure enhanced compaction. It is possible that reactive hot-spots which originate in the vicinity of metal particles may be intensified by exothermic metal oxidation reactions, thereby facilitating transition to global ignition by hot-spot growth and coalescence, provided that the heat generation rate is sufficient to overcome thermal conduction losses and prevent quenching.

5. **The dependence of shock profiles on the local friction coefficient was examined.** [Chakravarthy, et. al., 2010; Chakravarthy and Gonthier, 2010; Gonthier, 2010; Chakravarthy and Gonthier, 2011; Chakravarthy, et al., 2013 A; Chakravarthy, 2014] Friction work occurring in the vicinity of interparticle contacts is an important mechanism for the formation of small but intense hot-spots that result in local ignition. Though several studies have investigated the role of frictional heating in the ignition of energetic solids based on Coulomb-type models, disparities exist in the reported value of friction coefficient. These values vary over the range $0.1 \leq \mu \leq 1.1$ for mixtures containing common explosives such as HMX, PETN, RDX, and TNT that are in sliding contact with boundaries. Specifying an appropriate value of friction coefficient is complex, and depends on the thermomechanical properties of the mixture and boundary, the mixture-boundary slip velocity, the applied normal stress, and the temperature. Because of this complexity, and because many of these studies focus on frictional heating along macroscale boundaries rather than local interparticle contacts, it is desirable to examine how the value of friction coefficient affects bulk wave propagation and hot-spot formation within large particle ensembles. To this end, predictions were obtained for several values of friction coefficient within the range $0 \leq \mu \leq 1$ for $U_p = 500$ m/s and $\lambda_m = 0.2$. For simplicity, the

value of μ was taken to be constant for a given simulation and independent of the type of interparticle contact (e.g., HMX-HMX, metal-metal, or HMX-metal).

Predicted Hugoniot in the U_p - D and U_p - \bar{P} planes vary with μ . Uniaxial wave speed D monotonically increases with μ for strength dominated shocks as the rigidity of the ensemble is enhanced by interparticle friction, whereas friction only minimally affects D for pressure dominated shocks. The relation $D = D(U_p)$ is approximately linear for frictionless contact ($\mu = 0$) suggesting that phenomena or microstructural features that enhance particle mobility may give rise to a similar result; such phenomena/features might include particle fracture with subsequent rearrangement, 3D microstructures, or microstructures having higher initial porosity. The effective pressure is found to be insensitive to variations in μ for both strength and pressure dominated shocks.

Explosive hot-spot mass within and behind pressure dominated shocks also varies with μ . The high temperature tail of the explosive hot-spot mass fraction curve is absent for frictionless contact ($\mu \equiv 0$). As the value of friction coefficient increases, high temperature heating quickly intensifies until a value of $\mu \approx 0.1$ is reached; further increases in the value of μ over the approximate range $0.1 \leq \mu \leq 0.6$ have little additional effect on the high temperature tail. Values of $\mu > 0.6$, which result in frictionally rigid ensembles, reduce interparticle slip causing a slight reduction in the intensity of high temperature mass. This non-monotonic variation in frictionally induced heating with μ indicates the importance of properly describing surface dissipation as a hot-spot formation mechanism responsible for local ignition. Most mass affected by plastic work is largely insensitive to variations in μ , though small amounts of mass (e.g., $\lambda \approx 10^{-3}$) are heated to marginally higher temperatures because tangential (shear) stresses are more effectively transmitted between particles as μ increases causing frictionally enhanced plasticity. Qualitatively similar predictions were obtained for all shock strengths considered in this effort.

3 Analysis of Hot-Spots in Low Density Granular Explosives

3.1 Significance

Various micromechanical mechanisms of shock induced hot-spot formation have been postulated. Representative mechanisms include frictional heating due to sliding contact, shear band formation, rapid compressive heating of gas contained within voids during void collapse, and visco-plastic heating of solid material during void collapse. Which mechanism(s) dominates will depend on the material microstructure, the thermo-mechanical properties of the material constituents, and the loading conditions. Moreover, significant fluctuations in stress and temperature fields behind shocks due to material heterogeneity can give rise to complex hot-spot morphologies. Here, hot-spot morphology refers to geometrical characteristics such as size and shape which, along with intensity, establishes their criticality (i.e., the likelihood of locally experiencing thermal explosion). Because most analyses typically assume a simple pore geometry and a single formation mechanism, or because they focus on the shock response of a single hot-spot, they do not provide detailed statistical information on the formation of hot-spots behind shocks. Mesoscale M&S can principally account for hot-spot formation and provide statistically meaningful information on hot-spot intensity, size, and number that is important for ignition and flame spread [3, 1, 11]. These simulations computationally track the nonlinear deformation and motion of individual particles, and interactions between particles, enabling the spatial and temporal evolution of hot-spot fields behind shocks and

their combustion implications to be assessed. This effort represents a fundamental advancement in the characterization of how material microstructure can influence fine-scale dissipative heating within compaction shocks in low density explosives.

3.2 Goals and Methods

The key goal of this effort was *to computationally examine how initial porosity, metal mass fraction, and metal particle size affect shock induced hot-spot formation*. As shown in the previous section, the initial porosity of granular explosives has a leading-order effect on sensitivity, but the dissipative mechanisms responsible for hot-spot formation and their dependence on microstructure, composition, and shock strength remain vague. Importantly, the intensity, size, and spatial proximity of hot-spots, and the degree of mechanical and thermal confinement, will likely control the rate of hot-spot growth and coalescence; therefore, these features represent precursors to the onset of vigorous combustion.

The computational model used for mesoscale M&S of compaction shocks in granular explosives was described in Section 2.2. Because a key objective of this effort was to characterize hot-spots, a thresholding technique was developed to identify them based on computed temperature fields within particles behind shocks. To this end, hot-spot material was selected by performing a level-cut through $T(\mathbf{x}, t)$ at a predefined threshold temperature T_{th} ; the term *hot-spot* refers to material having $T \geq T_{th}$. The resulting level-cut, illustrated in Fig. 5, produces a *hot-spot temperature field* that contains N hot-spots, $\hat{\mathcal{A}}^1(\mathbf{x}, t), \hat{\mathcal{A}}^2(\mathbf{x}, t), \dots, \hat{\mathcal{A}}^N(\mathbf{x}, t)$, enclosed by contours $\Gamma^1(\mathbf{x}, t), \Gamma^2(\mathbf{x}, t), \dots, \Gamma^N(\mathbf{x}, t)$. This thresholding technique partitions the domain $\mathcal{A}(\mathbf{x}, t)$, into two disjoint sets, $\mathcal{A}_{HS}(\mathbf{x}, t)$ and $\overline{\mathcal{A}_{HS}}(\mathbf{x}, t)$, such that $\mathcal{A}_{HS}(\mathbf{x}, t) \cup \overline{\mathcal{A}_{HS}}(\mathbf{x}, t) = \mathcal{A}(\mathbf{x}, t)$ and $\mathcal{A}_{HS}(\mathbf{x}, t) \cap \overline{\mathcal{A}_{HS}}(\mathbf{x}, t) = \emptyset$, where $\mathcal{A}_{HS}(\mathbf{x}, t) = \hat{\mathcal{A}}^1(\mathbf{x}, t) \cup \hat{\mathcal{A}}^2(\mathbf{x}, t) \cup \dots \cup \hat{\mathcal{A}}^N(\mathbf{x}, t)$. The region $\mathcal{A}_{HS}(\mathbf{x}, t)$ contains all hot-spot material in $\mathcal{A}(\mathbf{x}, t)$ for a given material realization and piston speed, while the region $\overline{\mathcal{A}_{HS}}(\mathbf{x}, t)$ contains lower temperature material. This technique filters out cooler material allowing for a quantitative description of hot-spot features. It is noted that hot-spot morphology is sensitive to simulation resolution and the choice of T_{th} . In this study, $T_{th} = 500$ K was chosen which is slightly above the β - δ phase transition temperature of HMX; as such, this value reasonably indicates the onset of chemical activity, though exothermic combustion requires $T > T_{th}$ and is dependent on hot-spot size.

A complete statistical description of hot-spots requires that the hot-spot temperature field be analyzed for every realization of a material and subsequently averaged over all realizations. Because this requirement is computationally expensive, ergodicity was assumed which stipulates that averaging over all realizations of an ensemble is equivalent to averaging over the volume of a single realization in the infinite volume limit [16]. Though computational domains used in this study were finite, they were sufficiently large so that this assumption is reasonable in establishing the statistical features of hot-spots. Computational experiments performed for different realizations of a material having $\bar{\phi}_{s0} \approx 0.7$ confirmed this assertion. Detailed expositions of this work can be found in the cited references.

3.3 Work Accomplished

Hot-spots induced by compaction shocks were computationally examined for both HMX and HMX-Al composites. Also, a preliminary analysis was performed to explore how hot-spot formation rates induced by shocks can be used to establish an ignition criterion for low density HMX. Such a criterion can be used in the development of microstructure-dependent ignition and burn models

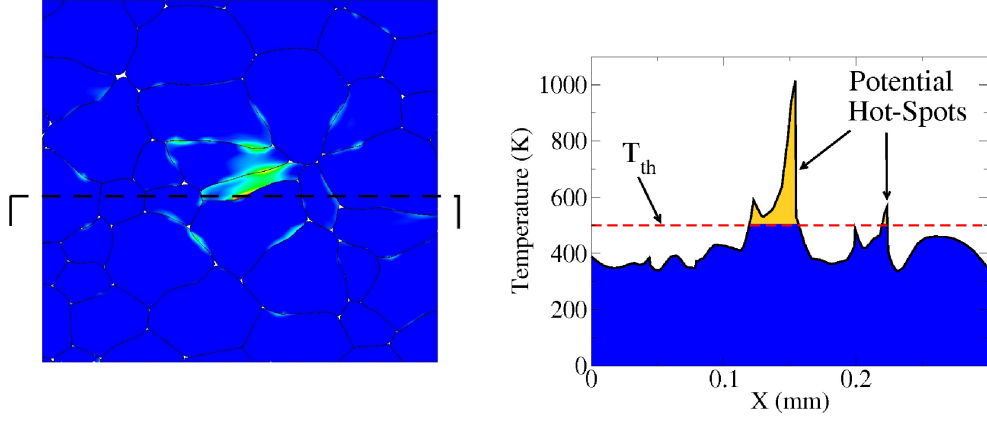


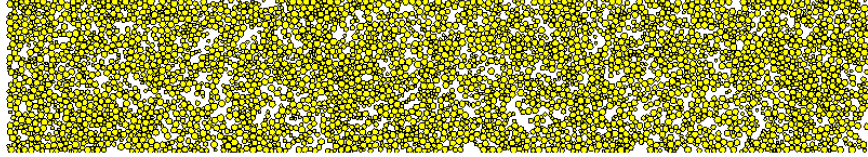
Figure 5: Illustration of the temperature thresholding technique used to identify hot-spots. Here, $T_{th} = 500$ K denotes the temperature threshold.

for assessing transition to detonation, as addressed in Section 4 of this report. Work accomplished as part of this effort along with key observations are briefly summarized below. Publications and presentations resulting from this work are indicated by the cited references.

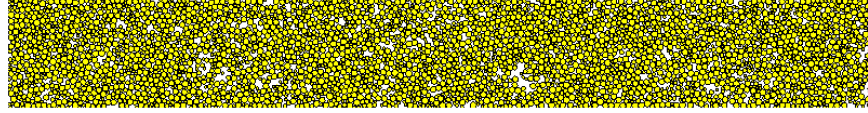
1. **The influence of particle packing density on hot-spot formation in low density HMX was computationally examined.** [Gilbert, 2012; Gilbert and Gonthier, 2012; Chakravarthy, et al., 2013 B; Gilbert, et. al., 2013] Emphasis was placed on examining how the material's initial particle packing density, characterized by its effective solid volume fraction $\bar{\phi}_{s,0}$, affects hot-spot statistics for pressure dominated waves corresponding to piston speeds within the range $300 \leq U_p \leq 500$ m/s. Figure 6 shows representative initial particle ensembles simulated in this effort. Ensembles consisted of hexagonally and/or circularly shaped, randomly packed, HMX particles having diameters of $40 \mu\text{m}$, $60 \mu\text{m}$, and $80 \mu\text{m}$ in equal ratios. The distribution in solid volume fraction within each ensemble was nearly Gaussian, and its standard deviation decreased with increasing density.

Analysis of temperature field predictions indicate that hot-spot intensity is only marginally affected by changes in impact speed, initial porosity, and particle shape for $0.57 \leq \bar{\phi}_{s,0} \leq 0.84$, with higher temperature scatter existing for highly porous material due to the wider distribution of initial pore sizes. Unlike intensity, hot-spot morphology and spatial proximity vary more appreciably. Figure 7 summarizes the predicted variation in hot-spot number density, volume fraction, and specific surface area with U_p for each ensemble. These quantities, expressed per unit total volume of material behind the shock, are often explicitly or implicitly used to describe ignition phenomena in macroscale burn models. An exponential growth in each of these quantities is predicted over the range of piston speeds considered. Importantly, these quantities exhibit a nonlinear dependence on $\bar{\phi}_{s,0}$: packing densities within the range $0.68 < \bar{\phi}_{s,0} < 0.84$ result in substantially fewer hot-spots at a given impact speed, whereas no appreciable changes are predicted for approximately $0.68 \leq \bar{\phi}_{s,0} \leq 0.58$. This latter prediction is consistent with shock sensitivity data for neat granular explosives which indicate little variation in sensitivity with porosity for highly porous materials. The slopes of curves corresponding to different ensembles are similar, with the exception of hot-spot number density which has a lower rate of increase with U_p for highly porous material due to the clustering

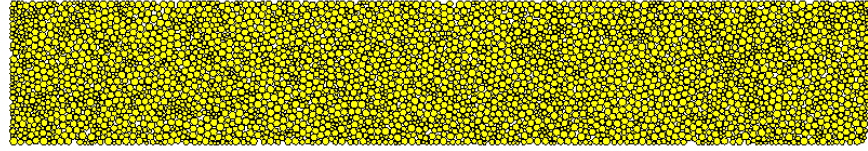
Meso-Structure A
($\bar{\phi}_{s,0} = 0.584$)



Meso-Structure B
($\bar{\phi}_{s,0} = 0.678$)



Meso-Structure C
($\bar{\phi}_{s,0} = 0.768$)



Meso-Structure D
($\bar{\phi}_{s,0} = 0.835$)

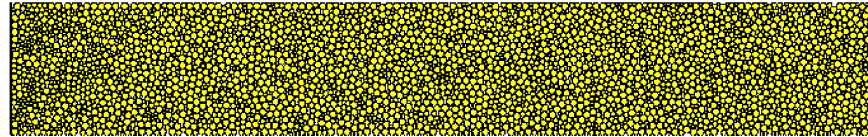


Figure 6: Representative initial particle ensembles used with mesoscale M&S to assess the effect of packing density on hot-spot formation in low density HMX.

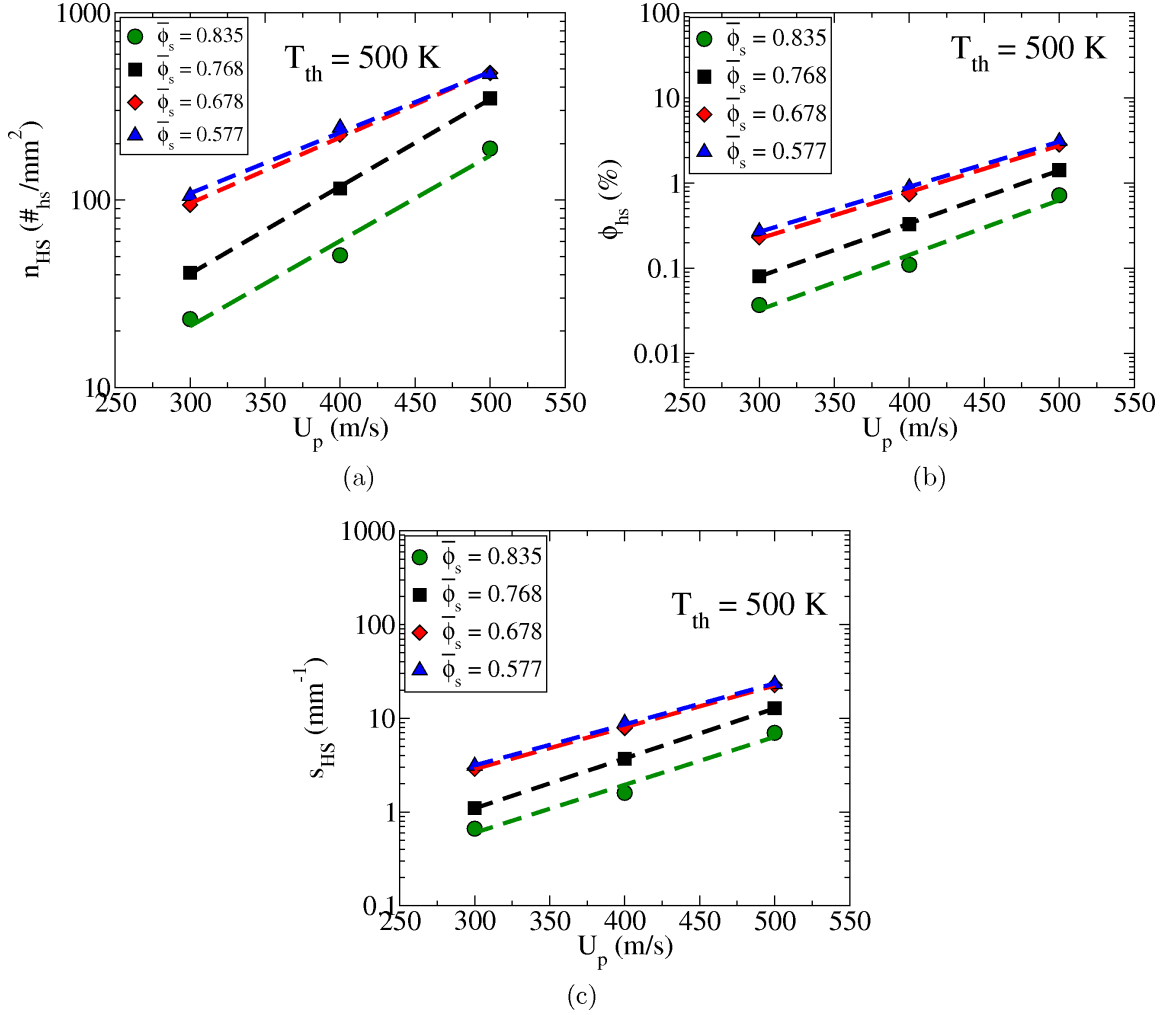


Figure 7: Predicted variation in (a) hot-spot number density, (b) hot-spot volume fraction, and (c) hot-spot specific surface area for each ensemble with piston speed. The dashed lines represent best-fit exponential functions.

and coalescence of hot-spots at higher impact speeds; i.e., hot-spots coalesce as more material is heated to elevated temperature, and their number density decreases. This observation is further addressed in Item 2 of this section.

The effective volumetric strain $\epsilon_V = 1 - \bar{\rho}_0/\bar{\rho}$ is influenced by both U_p and $\bar{\phi}_{s,0}$, where $\bar{\rho}$ is the effective material density. For pressure dominated shocks having $\bar{\phi} \approx 1$ with a stiff solid equation of state so that solid density changes are small, the effective volumetric strain may be approximated by $\epsilon_V \approx 1 - \bar{\phi}_{s,0}/\bar{\phi}_s \approx 1 - \bar{\phi}_{s,0}$ which is the initial porosity. Predicted deformation and temperature fields appreciably differ depending on $\bar{\phi}_{s,0}$ with high volumetric deformation resulting in larger, more densely packed hot-spots having a higher surface area/volume ratio. Consequently, the gas phase production rate responsible for the onset of vigorous combustion behind sustained shocks is more likely to be controlled by hot-spot morphology, proximity, and number rather than temperature-dependent chemistry.

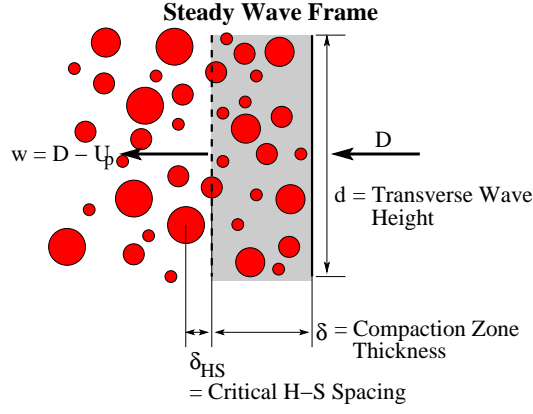


Figure 8: An illustration of hot-spot axial spacing used to compute the formation time between successive hot-spots based on their centroid locations.

Though speculative in the absence of coupled multiphase transport and chemistry, a similar description has been postulated to explain shock sensitivity data for preheated TATB-based explosives. These results suggest that the observed increase in sensitivity with initial porosity for sustained loading is likely due to an increase in hot-spot size and number rather than intensity.

2. **The dynamics of hot-spots in low density HMX was characterized in terms of increasing shock strength.** [Chakravarthy, 2014; Gonthier and Chakravarthy, 2014; Rao and Gonthier, 2015 A] This analysis focused on describing how hot-spots evolve with compaction shock strength; therefore, it was convenient to analyze hot-spots in a wave-attached frame, as conceptually shown in Fig. 8. In this frame, unstressed porous material enters the wave at speed D and stressed compacted material leaves the wave at speed $w = D - U_p$, where U_p is the piston speed and D is the corresponding steady wave speed. The spatial shock structure has a finite thickness δ due to energy dissipation and dispersion within the wave. Though the compacted state possesses fluctuations in thermomechanical fields, its effective pressure or temperature can be used to characterize shock strength. Hot-spots are formed within the shock due to inelastic pore collapse, emerging from the shock at a frequency that depends on both the mesostructure and shock strength.

Individual hot-spots are identified by the location of their area centroids enabling the formation rate to be characterized based on hot-spot spacing. Though other metrics may be used to characterize spacing (e.g., surface-to-surface nearest neighbor distributions, point-to-surface distributions, etc.), numerical experiments indicate that the formation rate is largely insensitive to the choice of metric for shocks dominated by hot-spot nucleation, as discussed below. For a given simulation, the formation time, defined as the time between successive formation of hot-spots within the shock, is estimated by $\tau_f \equiv \delta_{HS}/(D - U_p)$, where δ_{HS} is the axial distance between their centroids in the compacted state identified in Fig. 8. The transverse distance between hot-spots is not used to compute the distribution of formation times, but is implicitly accounted for by expressing the effective formation rate as an intensive quantity using the transverse wave dimension d in the analysis that follows.¹ Development

¹The wave dimension d is given by the transverse width of the computational domain.

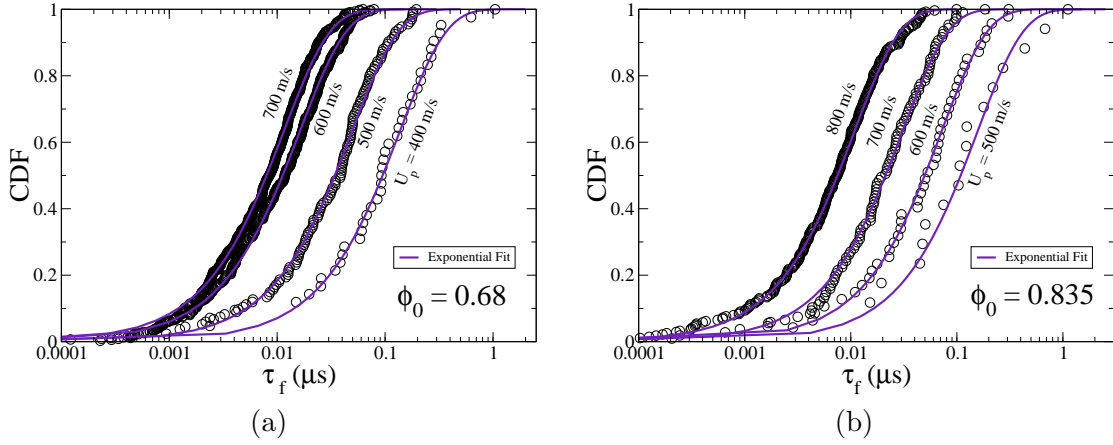


Figure 9: Predicted variation in hot-spot formation time distribution with U_p for steady waves in porous HMX: (a) $\bar{\phi}_0 = 0.68$; (b) $\bar{\phi}_0 = 0.84$.

of a technique that explicitly accounts for the average transverse spacing between hot-spots is a current topic of our ongoing research. This definition of τ_f , which establishes the effective formation rate, is influenced by both hot-spot spacing and wave speed. It is plausible that mesostructures having comparable hot-spot spacing but different wave speeds will have different ignition times because their formation rates will differ.

Figure 9 illustrates predicted distributions in hot-spot formation time for steady shocks in porous HMX. The distribution is dependent on both shock strength and mesostructure, characterized by $\bar{\phi}_0 = 0.68$ and 0.84 . Because simulations of weak impact require long computational domains to obtain statistically significant numbers of sparsely distributed hot-spots, this analysis focuses on shocks corresponding to $U_p \geq 400$ m/s which have sufficient strength to eliminate porosity. Formation time distributions are approximately exponential indicating that hot-spot formation represents a time-invariant Poisson process for mesostructures considered in this effort. The cumulative exponential distribution function is given by $F(\tau_f) = 1 - \exp(-\bar{\lambda}\tau_f)$, where $\bar{\lambda}$ is the effective formation rate/frequency of hot-spots. Because the mechanics of hot-spot formation depend on the interparticle contact geometry, hot-spot formation times may be strongly influenced by the particle size distribution.

Predicted variations in $\bar{\lambda}$ with shock strength and mesostructure, summarized in Fig. 10 in terms of U_p for $\bar{\phi}_0 = 0.68, 0.77$, and 0.84 , can provide insight into the dynamics of hot-spot formation within shocks that may have ignition implications. The dynamics involves a competition between the nucleation, growth, and agglomeration of hot-spots as shock strength increases. Here, nucleation refers to the formation or seeding of new hot-spots in the vicinity of interparticle contact surfaces, whereas growth and agglomeration refer to an increase in hot-spot size and the coalescence of neighboring hot-spots due to uncontained plastic flow, respectively.² For each material, an exponential increase in $\bar{\lambda}$ is initially predicted with increasing U_p due to the influence of hot-spot nucleation, with higher porosity resulting in a higher formation rate for fixed U_p . As U_p further increases, neighboring hot-spots begin

²Because reactive hot-spots are identified by their area centroids in this analysis which is independent of their size, agglomeration can cause in a reduction in $\bar{\lambda}$ when it dominates nucleation.

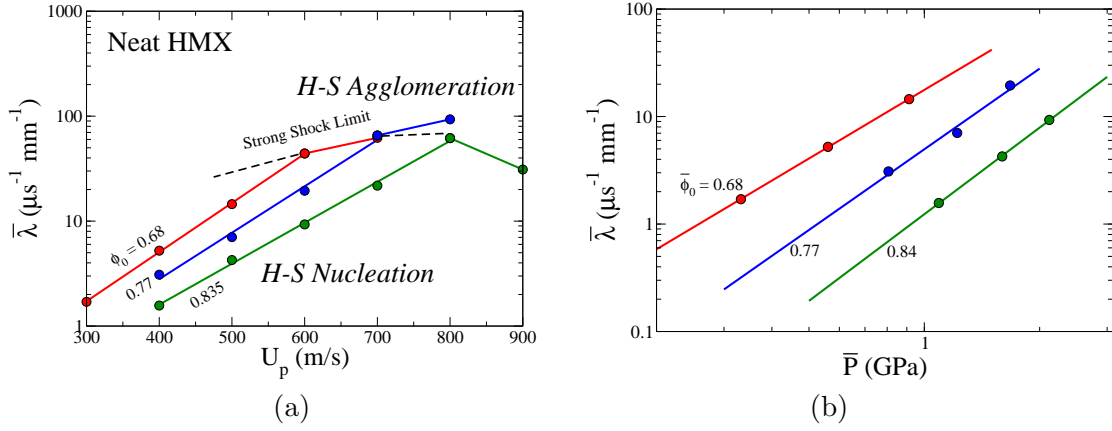


Figure 10: Predicted variation in the effective hot-spot formation rate with (a) piston speed and (b) shock pressure for low density HMX.

to coalesce/agglomerate resulting in slower increases in $\bar{\lambda}$; the value of U_p associated with the onset of this “strong shock” regime increases with $\bar{\phi}_0$. In this regime, the value of $\bar{\lambda}$ may decrease with a further increase in wave strength as agglomeration begins to dominate nucleation and hot-spots become ubiquitous within the material; this scenario is illustrated by the case corresponding to $U_p = 900$ m/s and $\bar{\phi}_0 = 0.84$. It is plausible that waves within the strong shock regime will result in prompt ignition and vigorous burn of material due to the close spatial proximity of large and intense hot-spots.

3. **The effective hot-spot formation rate in low density HMX can be expressed by a power-law relation in terms of shock pressure.** [Chakravarthy, 2014; Gonthier and Chakravarthy, 2014; Rao and Gonthier, 2015 A] It is desirable to express the formation rate in intensive form based on the wave frontal area. For the 2-D simulations performed in this study, the specific formation rate was defined by $\hat{\lambda} \equiv \bar{\lambda}/d$, where d is the transverse wave width. Therefore, $\hat{\lambda}$ represents the hot-spot number flux emerging from the wave. The formation rate was then related to shock pressure by the power-law expression $\hat{\lambda} = a\bar{P}^n$. The data and best-fit curves for each $\bar{\phi}_0$ are shown in Fig. 10 for the nucleation phase. Both the prefactor a and exponent n vary with initial packing density. As $\bar{\phi}_0$ increases for fixed \bar{P} , the effective bulk modulus of the material increases resulting in volumetric stiffening and faster waves, and reactive hot-spot spacing increases due to enhanced stress transmission between particles; consequently, $\hat{\lambda}$ decreases. However, because $n = \partial \log \hat{\lambda} / \partial \log \bar{P}$, the reactive hot-spot formation rate increases more rapidly with pressure for dense material, though it remains relatively low throughout the nucleation regime. This more rapid increase in formation rate with pressure for dense material is consistent with abrupt ignition once a critical threshold is obtained. These predictions indicate that the effective hot-spot formation rate is sensitive to material mesostructure and, therefore, may be a plausible measure for establishing a mesostructure-dependent ignition theory for macroscale modeling of low density granular explosives. This topic is further addressed in Section 4 of this report.
4. **A “ $P^n\tau$ -type” relation for the ignition time behind a shock was established based on a cumulative ignition function that depends on mesostructure through the effective hot-spot formation rate.** [Gonthier and Chakravarthy, 2014] The ignition relation

assumes that 1) ignition occurs during hot-spot nucleation so that the ignition time $\tau^* > \tau_r$, where τ_r is the shock rise time, and 2) $\tau^* \sim \hat{\lambda}^{-1}$. The first assumption restricts the analysis to shocks of intermediate strength that have an induction period prior to ignition due to growth and coalescence of initially small hot-spots by multiphase transport mechanisms. The second assumption is plausible because a large value of $\hat{\lambda}$ corresponds to the rapid formation of closely packed hot-spots that is likely to enhance the onset of ignition. Implicit in these assumptions is that waves resulting in significant hot-spot agglomeration due to widespread plasticity induce prompt ignition because $\tau^* < \tau_r$.

The cumulative hazard (ignition) function corresponding to an exponential distribution of hot-spot formation times for a shock characterized by $\hat{\lambda}$ is given by $\hat{\mathcal{I}}(\tau) = \int_0^\tau \hat{\lambda} d\tau' = \hat{\lambda}\tau$. Here, $\hat{\mathcal{I}}(\tau)$ represents the specific accumulation of hot-spots behind the shock over time. As a first approximation, it is assumed that ignition occurs behind the shock when $\hat{\mathcal{I}} = \hat{\mathcal{I}}^*$. The ignition time is given by $\tau^* = \hat{\mathcal{I}}^* \hat{\lambda}^{-1}$ which can be expressed in terms of \bar{P} and $\bar{\phi}_0$. The relation for ignition time is then given by $\bar{P}^n \tau^* = \frac{\hat{\mathcal{I}}^*}{a}$. The value of $\hat{\mathcal{I}}^*$ is estimated based on DDT data for porous HMX obtained by McAfee, et al. [10], which indicate that $\tau^* \approx 400 \mu\text{s}$ for $\bar{P} = 0.04 \text{ GPa}$, $\bar{\phi}_0 = 0.66$, and $\bar{d} = 125 \mu\text{m}$. Using these values with the power-law parameter values for $\bar{\phi}_0 = 0.68$, the estimate $\hat{\mathcal{I}}^* = 7.27 \text{ mm}^{-1}$ is obtained. Assuming this value to be a property of HMX, it is possible to estimate the variation in ignition time as a function of shock strength for different values of $\bar{\phi}_0$. This assumption is particularly reasonable for shocks considered in this study which have sufficient strength to eliminate porosity because the effect of residual porosity on flame spread leading to global ignition is inconsequential; therefore, the ignition time will be controlled to leading-order by the spatial proximity of reactive hot-spots in the completely compacted state and the rate at which they are formed.

Figure 11 illustrates the predicted variation in ignition time behind steady waves in porous HMX. Highlighted in red on the $\bar{\phi}_0 = 0.68$ curve is the single datum used to establish the value of $\hat{\mathcal{I}}^*$. Also highlighted in the figure is the approximate range of measured shock rise times reported by Sheffield, et al. [12], for porous HMX for shock strengths considered in this study ($0.07 \leq \tau_r \leq 0.7 \mu\text{s}$). Measurements indicate that shock rise time is largely insensitive to the value of $\bar{\phi}_0$. The predicted ignition time rapidly decreases with increasing wave strength for fixed $\bar{\phi}_0$. There exists a critical shock pressure that results in $\tau^* \approx \tau_r$ indicating the onset of prompt ignition within the wave; interestingly, this critical pressure approximately equals that required for the onset of hot-spot agglomeration. Using the terminology of Ref. [12], Region I identified in the figure, which corresponds to $\tau^* > \tau_r$, represents an ignition controlled process because of the long induction times, whereas Region II, which corresponds to $\tau^* < \tau_r$, represents a growth controlled process because the waves are sufficiently strong to induce prompt ignition. Measurements indicate that the reaction zone is strongly coupled to the shock front for growth controlled processes which is consistent with the estimates given here. Also shown in Fig. 11(b) are measured detonation initiation times reported by McAfee, et al., [10] and Dick [7] for $\bar{\phi}_0 \approx 0.68$. The relative difference between the ignition and initiation time increases with shock pressure indicating that reaction growth following ignition plays an increasingly important role in establishing the initiation time scale.

The relative shock sensitivity of explosives is frequently reported in the literature in terms of the axial run distance to detonation as a function of input shock pressure. Assuming that run

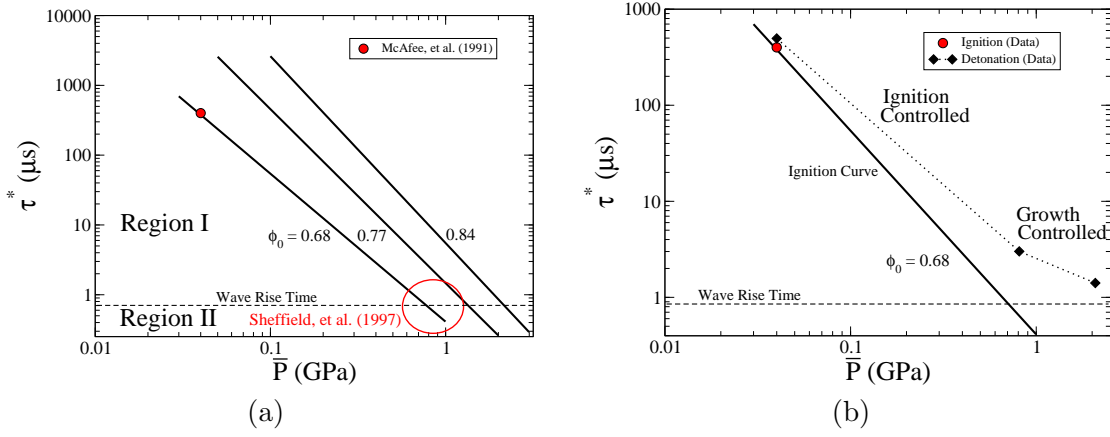


Figure 11: (a) Predicted variation in the global ignition time with wave strength for porous HMX having different values of $\bar{\phi}_0$. (b) Comparison of the predicted ignition curve with initiation time data for $\bar{\phi}_0 = 0.68$.

distance is a monotonic function of ignition time, then it is possible to qualitatively compare measurements of run distance to ignition time predictions. In particular, measurements on low density HMX indicate that the run distance to detonation increases with $\bar{\phi}_0$ for fixed shock pressure, and that it is slightly more sensitive to variations in pressure for dense material [8, 12]. Predicted ignition time curves reflect both features, where the increase in pressure sensitivity is due to the increase in the value of power-law exponent n with $\bar{\phi}_0$. These results were used to establish an ignition and burn model for describing the shock initiation of low density HMX, as discussed in Section 4 of this report.

5. **The influence of particle packing density on hot-spot formation in low density HMX-Al composites was computationally examined.** [Chakravarthy, 2014; Chakravarthy and Gonthier, 2016] Particle ensembles were considered in this effort that isolated the effects of initial particle packing density, characterized by the solid volume fraction ϕ_s , and aluminum mass fraction λ_m on shock sensitivity. Representative ensembles used with mesoscale M&S are shown in Fig. 12, where yellow particles are HMX and red particles are Al. The ensembles consisted of hexagonal and/or circular particles having an average diameter of $60 \mu\text{m}$ with a narrow distribution. The effective packing density was varied over the range $0.678 \leq \bar{\phi}_s \leq 0.835$. An effective metal mass fraction of $\lambda_m = 0.2$ was used for all ensembles. Impact speeds considered in this effort varied over the range $400 \leq U_p \leq 800 \text{ m/s}$ which resulted in pressure dominated shocks.

Figure 13 shows predicted Hugoniot. Here U_p and D are the piston and shock speed, respectively; $\bar{P} = (\bar{P}_e\phi_e + \bar{P}_m\phi_m)/(\bar{\phi}_e + \bar{\phi}_m)$ is the effective equilibrium mixture pressure behind the shock, where \bar{P}_e and \bar{P}_m are the explosive and metal pressures, and $\bar{\phi}_e$ and $\bar{\phi}_m$ are the explosive and metal volume fractions; and \bar{W}_{pe} is the effective dissipative work in the explosive component. Also shown are experimentally measured Hugoniot for neat HMX [12]. Predictions indicate that the inclusion of aluminum increases wave speed, pressure, and explosive dissipation for all cases compared to equivalent packing densities of neat HMX. However, little variation in explosive dissipation with shock pressure is predicted due to the increase in pressure with piston speed for HMX-Al mixtures. Shock rise times were found to decrease

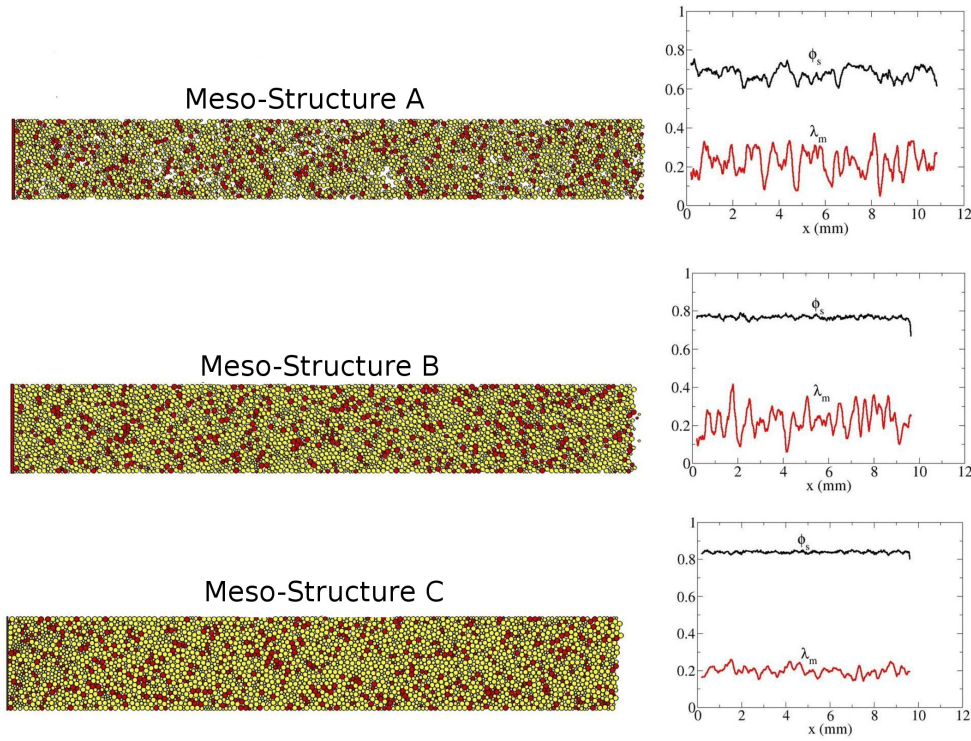


Figure 12: Initial particle ensembles with varying packing densities $\bar{\phi}_s$ and composition λ_m . Here, red particles represent Al, and yellow particles represent HMX.

with an increase in packing density and/or piston speed but were insensitive to variations in metal mass fraction.

An increase in packing density was found to increase the average HMX hot-spot size for fixed piston speed with only marginal variations in hot-spot intensity. The number density of hot-spots based on the total volume/area increases with piston speed for all packing densities prior to the onset of hot-spot agglomeration, whereas the volume fraction of hot-spots monotonically increases. Relative to neat HMX, the overall number density of hot-spots is lower due to spatial dilution.

When based on HMX volume and not total volume, qualitatively different behavior is predicted. Hugoniot were used to correlate hot-spot number density and volume fraction (based on HMX volume) with shock pressure, as shown in Fig. 14. Aluminized HMX is predicted to slightly suppress hot-spot formation relative to neat HMX for low pressure shocks associated with the nucleation and growth phases of hot-spot formation; thus, both the explosive hot-spot number density and volume fraction marginally decrease with metal addition. For low pressure shocks, where surface dissipation due to friction and/or localized plasticity are primary heating mechanisms, metal-explosive contact surfaces act as energy sinks due to the high thermal conductivity of aluminum which suppresses hot-spot formation. As shock pressure increases into the agglomeration phase of hot-spot formation, uncontained plasticity within explosive particles becomes a primary heating mechanism which is enhanced by intense shock reflections from explosive-aluminum interfaces. Moreover, this effect is predicted to increase

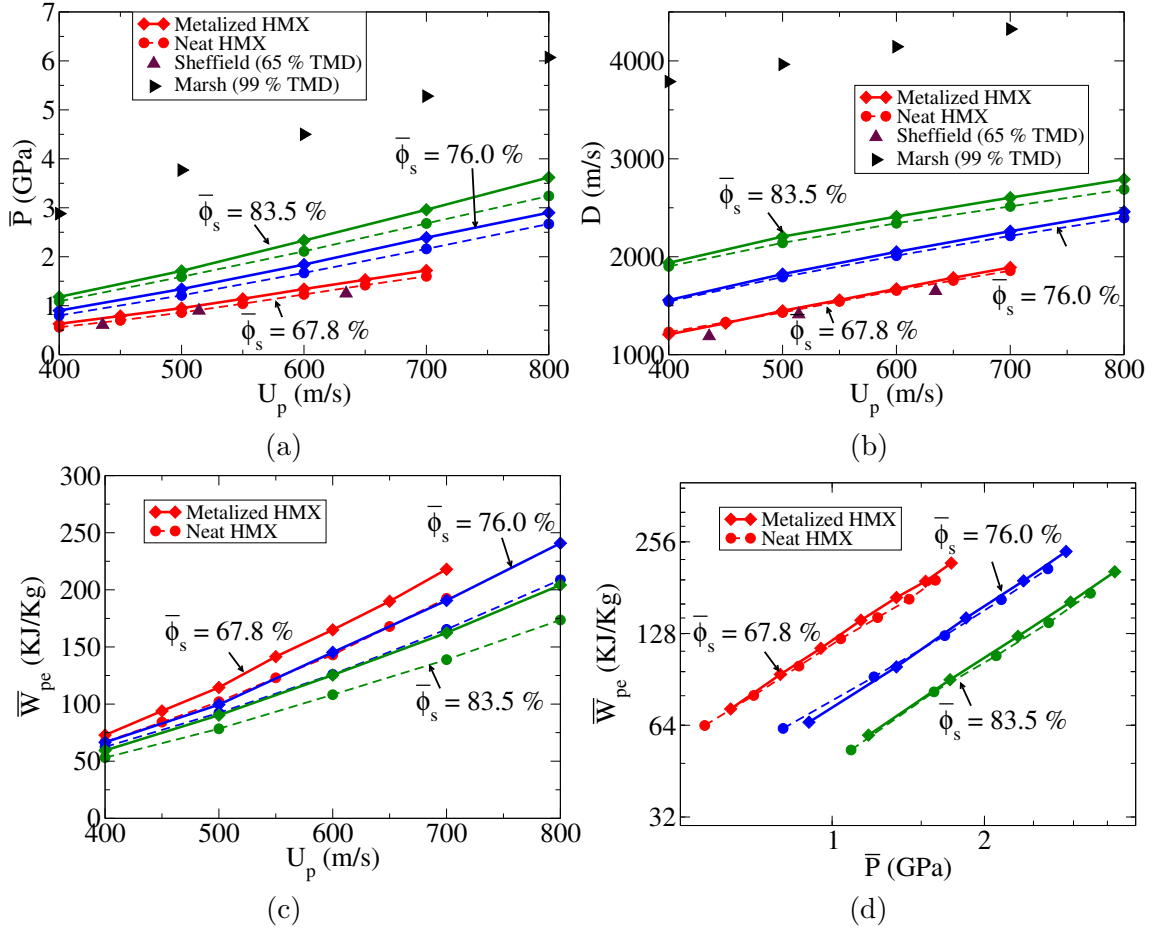


Figure 13: Predicted variations in effective shock end states as function of $\bar{\phi}_s$ and λ_m : (a) \bar{P} - U_p ; (b) D - U_p ; (c) \bar{W}_{pe} - U_p ; and (d) \bar{W}_{pe} - \bar{P} .

with particle packing density. These predictions suggest that the inclusion of aluminum in low density composites may delay HMX ignition for low pressure shocks.

- The influence of particle size on hot-spot formation in low density HMX-Al composites was computationally examined.** [Chakravarthy, 2014; Chakravarthy and Gonthier, 2016] Mesoscale M&S was performed to characterize how disparities between the average HMX and aluminum particle size affect explosive hot-spot formation. To this end, aluminum/HMX particle size ratios of 1, 2, 3, and 6 were considered for aluminum mass fractions of $\lambda_m = 0.20$ and 0.56 , and a solid volume fraction of $\bar{\phi}_s = 0.84$. All particle size distributions were narrow, and the average HMX particle size was approximately $60 \mu\text{m}$ for all cases. These particle size ratios were largely chosen based on computational constraints. Representative particle ensembles are shown in Fig. 15.

Predictions indicate that aluminum particle size has a largely inconsequential effect on shock Hugoniots for material having $\lambda_m = 0.20$, as illustrated by the variation in explosive dissipative work with shock pressure in Fig. 16(a). Compaction shock Hugoniots are more strongly influenced by aluminum particle size for materials having higher aluminum mass, as illustrated in Fig. 16(b) for $\lambda_m = 0.56$, where a monotonic increase in shock pressure and dissipative work

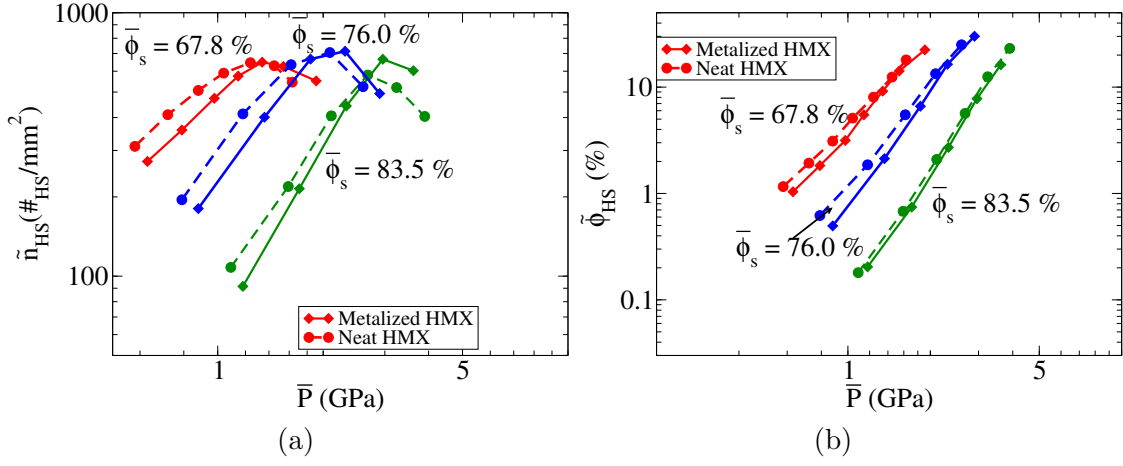


Figure 14: Predicted variations in the effective plastic work of the explosive component as a function of $\bar{\phi}_s$, and λ_m .

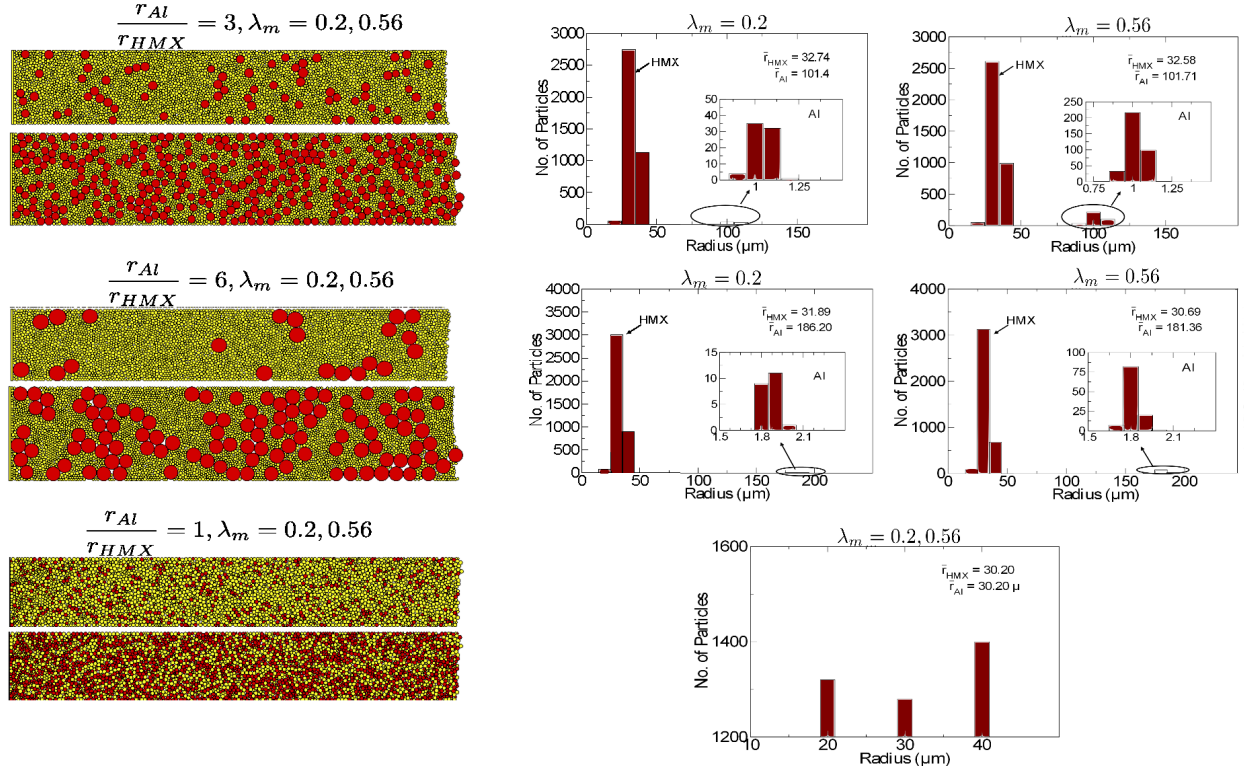


Figure 15: Meso-structures with varying particle sizes, particle distributions and composition. Here, red particles represent metal, and yellow particles represent explosive.

are predicted with an increase in Al particle size. Because this size effect is also predicted for identical particle ensembles of neat HMX, it is not dominated by the material make-up of the contacting surfaces. Additionally, smaller particles that are surrounded by larger particles can become pinched during shock passage resulting in higher local pressure and deformation; this pinching effect is enhanced in regions where small HMX particles are locally surrounded by large Al particles due to the high bulk modulus of aluminum.

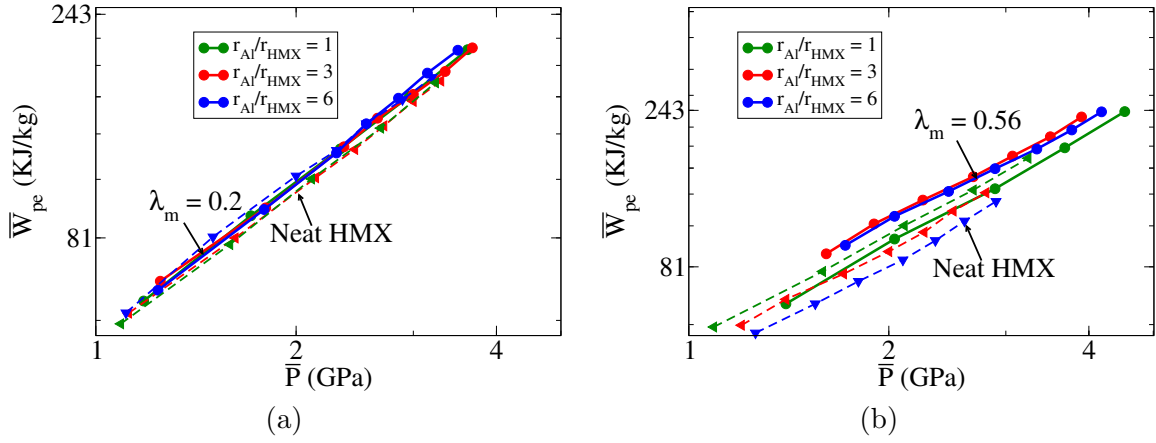


Figure 16: Predicted variations in explosive dissipative work with particle size ratio and shock pressure for a granular HMX-Al composite having $\bar{\phi}_s = 0.84$: (a) $\lambda_m = 0.20$ and (b) $\lambda_m = 0.56$.

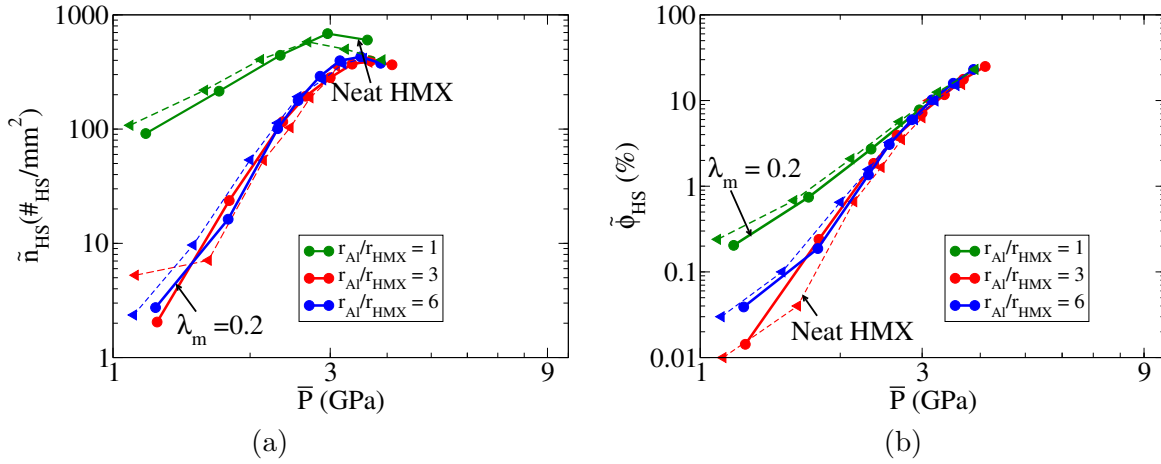


Figure 17: Predicted variations in hot-spot volumetric properties with particle size ratio and shock pressure for a granular HMX-Al composite having $\bar{\phi}_s = 0.84$ and $\lambda_m = 0.20$: (a) number density and (b) volume fraction.

Explosive hot-spot number density and volume fraction are predicted to have a strong non-linear dependence on Al particle size for low pressure shocks (approximately $\bar{P} < 2.5$ GPa for $\bar{\phi}_s = 0.84$), as illustrated in Fig. 17. An appreciable decrease in hot-spot number density and volume fraction is predicted for material containing large Al particles compared to material having equal particle sizes. Though speculative, it is plausible that frictional dissipation and/or localized plasticity which dominate the nucleation and early growth phase of hot-spot formation may be sensitive to minor changes in granular bed morphology. Marginal differences in hot-spot volume fraction, and larger differences in number density, are predicted for high pressure shocks. This prediction is due to uncontained plasticity and hot-spot agglomeration that occurs in the vicinity of large Al particles resulting in the formation of fewer but larger hot-spots. Similar trends are predicted for materials having $\lambda_m = 0.56$. Additional analysis is required to examine why disparate particle sizes can result in a significant decrease in hot-spot volumetric quantities at low shock pressures; this effect may have significant implications on the shock ignition of HMX-Al composites.

4 Ignition and Burn Modeling for Low Density HMX

4.1 Significance

Continuum theories are routinely used to examine shock initiation of solid explosives that occurs over length scales that are appreciably larger than the particle scale. These theories describe the effective/bulk response of the material and do not resolve the formation, growth, and interaction of reactive hot-spots within the microstructure. The relative importance of dissipation mechanisms, their dependence on microstructure and loading conditions, and their influence on macro-scale behavior remain fertile areas of research. Both mesoscale and macroscale M&S have been performed to address these and other issues, but these studies have largely focused on sustained single shocks to establish a foundation for analyzing more complex loading scenarios that may result in detonation. Successful application of commonly used hot-spot motivated burn models, such as Ignition and Growth [15], hinges on proper tuning of large parameter sets to initiation data. Though many parameters have a physical interpretation based on hot-spots, it can be difficult to establish their values in the absence of hot-spot and initiation data for specific microstructures under consideration. This effort represents a preliminary step toward the development of a simple technique to incorporate microstructure-dependent hot-spot features into ignition and burn models for low density explosives without the complexity of having to resolve particle scale ignition and burn.

4.2 Goals and Methods

The key goal of this effort was *to utilize results from mesoscale M&S discussed in Section 3 to formulate a microstructure-dependent ignition and burn model for low density HMX*. The model was used with a macroscale multiphase flow theory and a high-resolution computational technique to examine shock initiation. The model is conceptually similar to Ignition and Growth but accounts for ignition in terms of parameters that are explicitly determined from hot-spot fields.

The multiphase flow theory used in this effort is a two-phase limiting form of the more general multiphase model formulated by Crochet [5]. The vector form of the model equations in Cartesian coordinates are expressed as

$$\frac{\partial \mathbf{q}}{\partial t} + \frac{\partial \mathbf{f}(\mathbf{q})}{\partial x} = \mathbf{g}(\mathbf{q}) \frac{\partial \phi_s}{\partial x} + \mathbf{s}(\mathbf{q}). \quad (4)$$

Here, \mathbf{q} is the vector of conserved variables, $\mathbf{f}(\mathbf{q})$ is the flux vector, $\mathbf{g}(\mathbf{q})$ is the vector associated with nonconservative nozzling sources, and $\mathbf{s}(\mathbf{q})$ is the phase interaction source vector. These equations describe the evolution of mass, momentum, total energy, and solid volume fraction of the granular explosive. Complete details of the model, including constitutive relations for granular HMX, are given in Refs. [5, 6]. Development of the multiphase constitutive theory represents an additional contribution of this effort as per Item 3 below. All mesoscale M&S performed in this effort was based on the model and numerical technique discussed in Section 2. Both inert and reactive shocks in low density HMX were examined. Comparisons between mesoscale predictions of effective shock profiles and those given by the multiphase theory for inert shocks were examined to assess their agreement, particularly in terms of dissipation; this assessment was important because it enables particle scale behavior to be interpreted within the context of multiphase theory predictions.

4.3 Work Accomplished

Work accomplished as part of this effort along with key observations are briefly summarized below. Publications and presentations resulting from this work are indicated by the cited references.

1. **An analysis of compaction wave dissipation in low density HMX was performed.** [Rao and Gonthier; 2014 A; Rao, et al., 2013; Rao and Gonthier, 2016] Mesoscale M&S was performed to computationally examine how initial porosity influences dissipation rates within inert compaction shocks and to compare predictions to a continuum compaction theory. Effective shock profiles were obtained by averaging meso-scale fields over space and time. The continuum theory directly predicts the variation in effective thermomechanical fields during compaction due to an imbalance between an effective solid pressure and a configurational stress.

A key focus of this effort was to examine dissipation within compaction shocks. The mass-specific deformation power prescribed by the mesoscale model [Section 2] is expressed by

$$\mathcal{P} = \frac{1}{\rho} (\boldsymbol{\tau} : (\mathbf{d} - \mathbf{d}_p)) + \frac{P}{\rho} \text{tr}(\mathbf{d} - \mathbf{d}_p) + \frac{1}{\rho} (\boldsymbol{\sigma} : \mathbf{d}_p). \quad (5)$$

Terms on the right side of this equation represent shear, compression, and plastic work rates, respectively. Within the context of this model, shear work results in a non-thermal change of stored strain energy, whereas compression and plastic work result in deformation induced heating. Only plastic work is dissipative in that it causes an irreversible production of entropy, with the local dissipation power given by

$$T\dot{\eta} = \frac{1}{\rho} (\boldsymbol{\sigma} : \mathbf{d}_p) \geq 0, \quad (6)$$

where η is the mass-specific entropy. Friction work occurring at inter-particle boundaries is also dissipative when slip occurs; the frictional dissipation power is locally given by $T\dot{\eta}_f = \mathbf{t}_c \cdot \mathbf{v}_r$, where \mathbf{v}_r is the relative slip velocity. Because frictional dissipation is localized at particle contact surfaces, it does not appreciably contribute to the effective (or bulk) mass-specific dissipated energy. Therefore, dissipated energy by plastic work dominates the effective response, though frictionally induced tangential surface tractions can indirectly contribute to dissipation by enhancing plastic deformation within particles. Dissipative work is obtained by integrating Eq. (6) in time.

The mass-specific deformation power prescribed by the continuum compaction theory is expressed by

$$\begin{aligned} \mathcal{P} &= \dot{B} + \dot{e}_\rho + \dot{e}_\phi + \dot{e}_{\tilde{\phi}} \\ &= \frac{\beta}{\rho_s \phi} \frac{d}{dt} (\phi - \tilde{\phi}) + \frac{P_s}{\rho_s^2} \frac{d\rho_s}{dt} + \frac{(P_s - \beta)}{\rho_s \phi} \frac{d\phi}{dt} + \frac{\beta}{\rho_s \phi} \frac{d\tilde{\phi}}{dt} \end{aligned} \quad (7)$$

where

$$\frac{d\phi}{dt} = \frac{\phi(1-\phi)}{\mu} (P_s - \beta), \quad (8)$$

$$\frac{d\tilde{\phi}}{dt} = \begin{cases} f'(\phi) \frac{d\phi}{dt} & \text{if } f(\phi) > \tilde{\phi} \\ 0 & \text{otherwise.} \end{cases} \quad (9)$$

Here, $d(\bullet)/dt \equiv \partial(\bullet)/\partial t + \mathbf{v} \cdot \nabla(\bullet)$ is the Lagrangian derivative. Terms on the left of the second equality in Eq. (7) are respectively defined by the corresponding terms on the right.

In Eq. (7), \dot{B} implicitly accounts for the rate of stored compaction energy at the particle scale due to shear, \dot{e}_ρ accounts for the compression work rate, and $\dot{e}_c = \dot{e}_\phi + \dot{e}_\phi^\gamma$ accounts for the compaction work rate. The term \dot{e}_c consists of both a rate-dependent component \dot{e}_ϕ , which vanishes in the slow compaction limit (i.e., $P_s \rightarrow \beta$), and an inelastic component \dot{e}_ϕ^γ . These contributions to the deformation power are respectively analogous to the integrated contributions of those given in Eq. (5) for the mesoscale description. The Second Law of Thermodynamics gives the strong form of the dissipation inequality

$$T_s \dot{\eta} = \dot{e}_\phi + \dot{e}_\phi^\gamma \geq 0, \quad (10)$$

where $\eta = \eta_s$ is the mass-specific granular solid entropy. The first term on the right side of this equation is non-negative, as is the second term because $\beta \geq 0$ and $d\tilde{\phi}/dt \geq 0$ by construction. This thermodynamic description is compatible with a Helmholtz free energy of the form $\psi(\rho_s, T_s, \phi, \tilde{\phi}) = \psi_s(\rho_s, T_s) + B(\phi - \tilde{\phi})$, where ψ_s is the mass-specific solid phase free energy. Here, ψ_s is the thermal component of free energy. Rate-dependent compaction is the dominate dissipation mechanism for compaction shocks because $\dot{e}_\phi \gg \dot{e}_\phi^\gamma$.

The analysis indicates that increasing porosity decreases the dissipative work rate within shocks but increases the integrated dissipative work over shock rise times which is indicative of enhanced sensitivity. Representative predictions for the dissipation rate and dissipative work profiles for a pressure dominated compaction shock corresponding to $U_p = 500$ m/s are shown in Fig. 18. Qualitative agreement between mesoscale and continuum theory predictions is reasonable, though quantitative discrepancies exist due to differences in their constitutive theories. Figure 19(a) illustrates a comparison between predicted variations in dissipative work with shock pressure and initial packing density; again, good qualitative agreement exist in all cases. The relation between dissipative work and shock pressure can be accurately described by a density-dependent power law. The continuum theory results in shock thicknesses that are comparable to those predicted by mesoscale M&S, where the thickness is largely independent of ϕ_0 , but appreciably decreases with increasing U_p , which is consistent with measured data for low density HMX. [12] A comparison between predicted shock rise times is given in Fig. 19(b).

2. **Rapid and successive inert shock loading of low density HMX was computationally examined.** [Rao and Gonthier, 2015 A] Shock compaction of granular explosives can trigger combustion that results in detonation, even for relatively mild shocks. It is well established that a primary (or lead) shock can desensitize the material to subsequent shocks by reducing porosity. This phenomenon, referred to as shock desensitization, has been observed during Deflagration-to-Detonation Transition (DDT) of low density granular explosives in which complex interactions between impact and combustion-supported shocks influence the initiation process. In this effort, a computational analysis was performed to characterize how rapid successive planar shock loading of low density HMX affects dissipation. Mesoscale M&S was used to predict effective shock profiles and to examine hot-spot fields induced by pore collapse. Resolved shock profiles were compared to those given by the continuum compaction theory, and both were analyzed in a thermodynamic space that highlights desensitization effects.

Figures 20(a) and (b) show the spatial variation in dissipated work w_d at various times following initial impact predicted by mesoscale M&S and the continuum compaction theory,

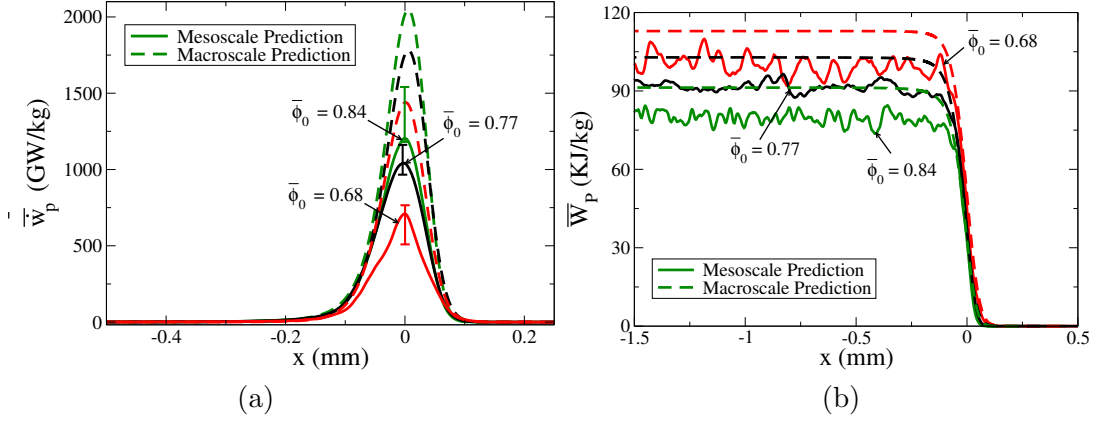


Figure 18: A comparison between mesoscale and continuum theory predictions for shock dissipation rate and dissipative work profiles corresponding to $U_p = 500$ m/s. Shock profiles are shown for different values of initial solid volume fraction $\bar{\phi}_0$. The shock is propagating from left to right in the figure.

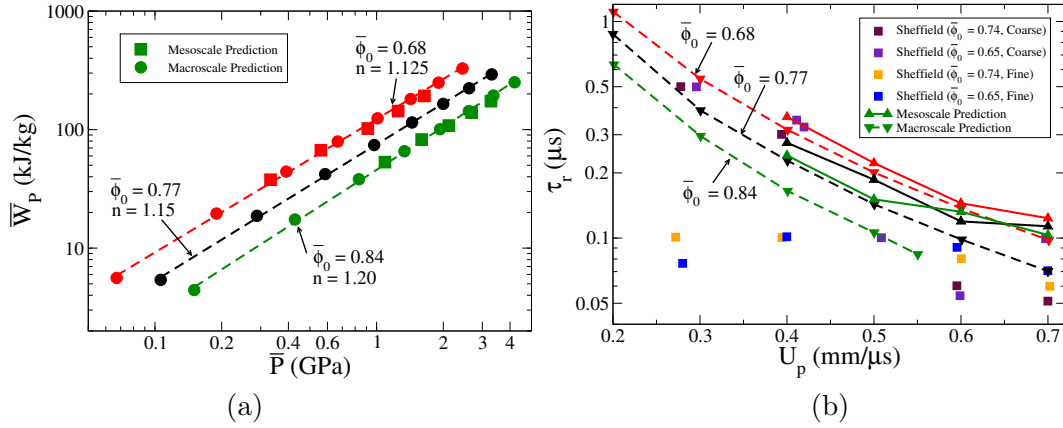


Figure 19: A comparison between mesoscale and continuum theory predictions for (a) the variation in effective dissipative work with shock pressure and (b) the variation in compaction shock rise time with supporting piston speed.

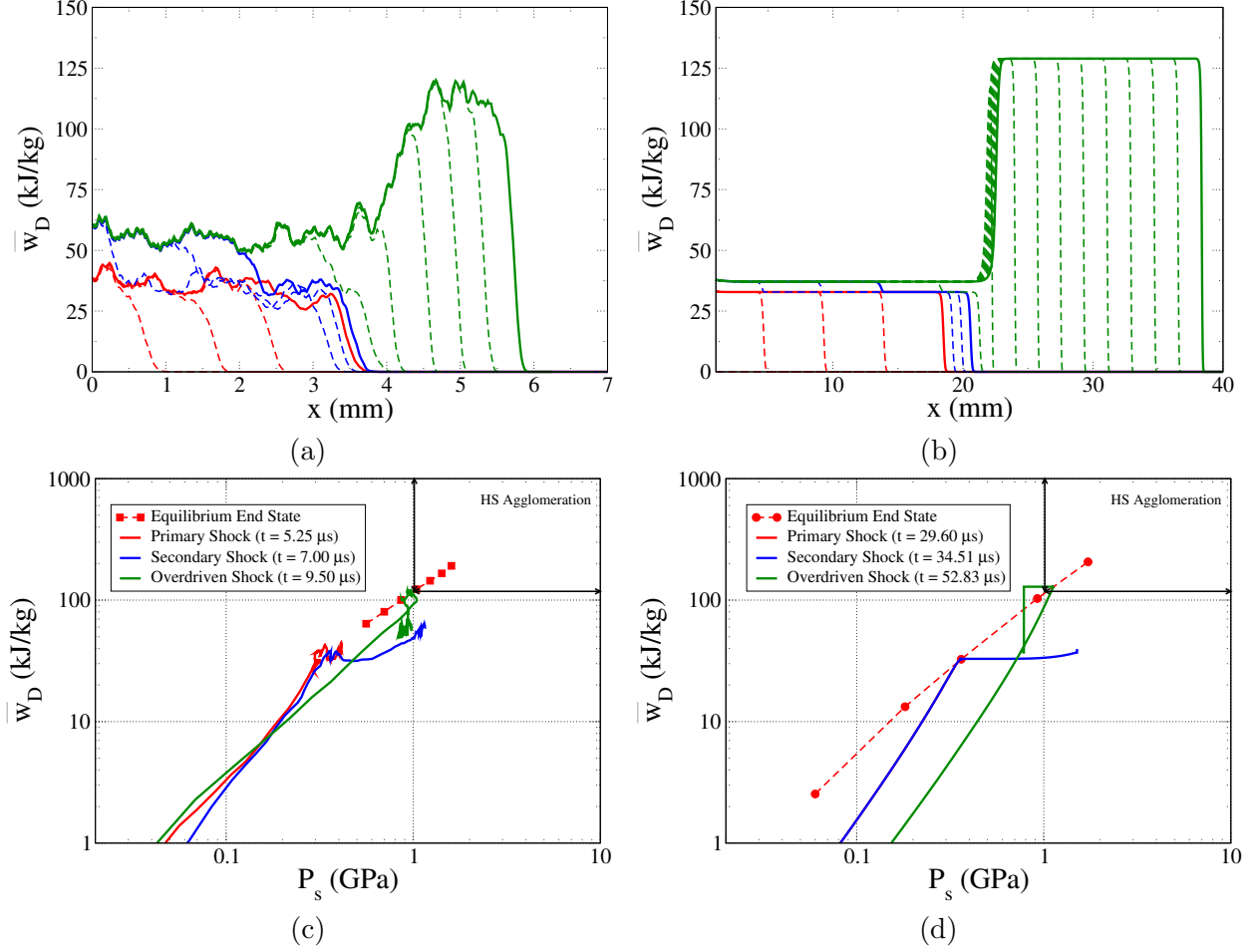


Figure 20: A comparison of mesoscale M&S and continuum compaction theory predictions for dissipative work profiles induced by successive planar shock loading of low density HMX having $\phi_0 = 0.68$. The successive supporting piston speeds are $U_{P1} = 300$ m/s and $U_{P2} = 500$ m/s. (a) Mesoscale and (b) continuum theory spatial fields at various times. Fields are plotted in a right propagating piston-attached reference frame; the piston surface is located at $\xi = 0$ mm. (c) Mesoscale and (d) continuum theory predictions plotted in pressure-dissipated work phase space.

respectively, for $\phi_0 = 0.68$. Corresponding times differ between the simulations due to differences in domain lengths and the time at which the piston speed transitions from U_{P1} to U_{P2} . In both cases, the lead compaction shock, which eliminates much of the initial porosity, propagates a relatively long distance into the domain before the piston speed increases to U_{P2} . Subsequently, a quasi-steady secondary shock quickly develops that eliminates residual porosity in material precompacted by the lead shock. The secondary shock is overdriven relative to the ambient material which has lower impedance than the denser material through which it propagates. Consequently, it experiences a gradual decay in pressure as it overtakes the lead shock and transits to the ambient material. The pressure decay predicted by mesoscale M&S is faster than that of the continuum theory due to its shorter domain length that facilitates rapid reverberation of release waves between the shock and piston. The shock transmission process is accompanied by a relatively modest increase in solid particle velocity and a substantial increase ($\approx 350\%$) in dissipative compaction work which mesoscale simulations indicate can result in ubiquitous formation of hot-spots. Mesoscale M&S and the continuum theory predict qualitatively similar features and exhibit reasonable quantitative agreement.

Figures 20(c) and (d) display the predictions of (a) and (b) in a phase space characterized by solid pressure P_s and w_d . This space is chosen because P_s represents a measure of shock strength and w_d represents a measure of hot-spot formation within the material. For comparative purposes, single shock end state predictions given by both descriptions are also shown in the figure. Mesoscale M&S of single shocks indicate that appreciable hot-spot agglomeration results for approximately $w_d > 100$ kJ/kg and $P_s > 1.6$ GPa for $\phi_0 = 0.68$; this region is also highlighted in the figure for reference. Though speculative in the absence of reactive mesoscale data, it is reasonable to expect that shocked material having tightly packed agglomerated hot-spots may significantly reduce reactive hot-spot interaction times, possibly resulting in prompt ignition and initiation. This assertion is consistent with the almost “discontinuous” initiation events observed by McAfee, et al., [10] during DDT in low density HMX resulting from the interaction of piston and combustion driven compaction shocks. Such observations reinforce the need to better characterize dissipation and ignition by rapid and successive shock loading of low density explosives.

Identified on the autonomous solution trajectories of Figs. (20)(c) and (d) are the equilibrium end states behind the lead and secondary quasi-steady shocks, where the lead shock end states lie on the single shock equilibrium curves. Unlike these autonomous solution trajectories, those associated with the interaction process between the lead and secondary shocks are time-dependent; only a single representative trajectory is shown for each of these processes in the plots. Again, mesoscale M&S and the continuum theory give comparable results. A few features are noteworthy. First, the lead shock strength is sufficient to eliminate most porosity resulting in relatively small additional increases in w_d by the secondary shock. Consequently, in all cases the value of w_d induced by the secondary shock is substantially lower than that induced by a single shock of equivalent pressure which is indicative of significant shock desensitization. Second, based on an analysis of hot-spots, appreciable agglomeration only results as the secondary shock overtakes the lead shock for the values of U_{P1} and U_{P2} imposed here. This prediction demonstrates how the strength of the secondary shock needed to induce agglomeration is dependent on the strength of the lead shock and the value of ϕ_0 . Third, increasing ϕ_0 tends to suppress dissipation and enhance desensitization.

3. **A multiphase theory for the detonation of low density explosives containing an arbitrary number of solid components was formulated.** [Crochet, et al., 2012; Crochet, 2013; Crochet and Gonthier, 2015] Multiphase continuum models are commonly used to predict the shock, combustion and detonation of granular energetic mixtures containing solid reactants and gaseous products. These models often include phase interaction terms that formally satisfy the strong form of the Second Law of Thermodynamics and provide flexibility in distributing dissipation between phases arising from non-equilibrium phenomena. This effort formulated a thermodynamically compatible constitutive theory for reactive systems containing an arbitrary number of solid components. The theory represents a rigorous extension of the two-phase theory formulated by Bdzil, et al. [4], based on the well-studied Baer-Nunziato model. Forms of the gas-solid and solid-solid interphase sources suggested by general reactions of type $A \rightarrow B$ are considered, where the combustion processes discussed in [4] are treated as a special case. The model energetics are augmented by supplemental evolutionary equations that track local changes in phase temperatures due to dissipative and transport processes allowing for the identification of dominant energetic processes. This capability provides a means to identify system parameters (e.g., metal particle size and mass fraction in metalized energetic mixtures) which optimize performance metrics. Predictions were obtained for mixtures of granular HMX and aluminum to demonstrate model features and to highlight the effect of aluminum particle self-heating by oxidation on detonation. Predicted spatial profiles for mechanical fields, and the heating contributions from individual dissipative processes, illustrated how aluminum particle size can affect the coupling of oxidative heating to the explosive reaction zone. This extended theory is currently being used by the PI to computationally characterize shock initiation of HMX-Al composites.
4. **A simple reactive burn model was formulated that describes shock induced combustion of low density HMX.** [Rao and Gonthier, 2014 B] The burn model incorporated the ignition criterion based on effective hot-spot formation rates discussed in Section 3 (Item 4). The effective rate was related to bulk wave pressure through a power law. The burn model was implemented in the two-phase (explosive and product gas) non-equilibrium continuum theory given by Eq. (4) to computationally examine how ignition and initiation vary with initial packing density and shock strength.

Of particular importance in this effort is the volumetric mass exchange term \mathcal{C}_s that governs the explosive combustion rate. It is common to take $\mathcal{C}_s = \mathcal{C}_s(\rho_s, \phi_s, P_g)$, where the functional dependency on gas pressure reflects strand burn data. Because ignition results from dissipative heating at the pore scale during shock compaction, it is plausible to use an expanded expression that accounts for the role of hot-spots in triggering ignition.

The ignition induction period behind shocks depends on both mesostructure and shock strength. To this end, Eq. (4) is supplemented by a history variable rate equation that describes the evolution of a dimensionless ignition variable λ_I :

$$\frac{d\lambda_I}{dt_s} = \frac{1}{t_r} \left(\frac{P_s - P_0}{P_r} \right)^m, \quad (11)$$

where t_r and P_r are a reference time and pressure, m is a history variable exponent, and P_0 (≈ 0 for this effort) is the ambient material pressure. The ignition variable is defined for $0 \leq \lambda_I \leq 1$, where $\lambda_I = 1$ denotes ignition. The solid pressure P_s is chosen as the history variable because it drives compaction induced dissipation which represents a primary

hot-spot formation mechanism in the continuum theory. Assuming a constant shock pressure and taking $t_s = 0$ at the shock front, Eq. (11) can be directly integrated to give $\lambda_I = (t_s/t_r)((P_s - P_0)/P_r)^m$, where t_s is time since shock passage for the explosive phase. For ignition, $\lambda_I = 1$ and $t_s = \tau^*$; also, $P_s \approx \bar{P}$ because $\phi_s \approx 1$ in the compacted state for shocks considered in this effort. Thus, using the criterion $\bar{P}^n \tau^* = \frac{\mathcal{I}^*}{a}$ from Section 3 (Item 4), and taking $m = n$, the expression $1 = (\tau^*/t_r)((P_s - P_0)/P_r)^n$ is obtained enabling Eq. (11) to be expressed as

$$\frac{d\lambda_I}{dt_s} = \begin{cases} \frac{a}{\mathcal{I}^*} (P_s - P_0)^n & 0 \leq \lambda_I \leq 1 \\ 0 & \text{otherwise} \end{cases}, \quad (12)$$

where the constant parameters a , \mathcal{I}^* , and n are mesostructure-dependent. The volumetric mass exchange term is then taken to be

$$\mathcal{C}_s = \begin{cases} 0 & \text{for } 0 \leq \lambda_I < 1 \\ \sigma \rho_s \phi_s P_g & \text{for } \lambda_I = 1, \end{cases} \quad (13)$$

where the constant σ is a burn prefactor. Here, it is assumed that negligible gas is produced during the induction period corresponding to $0 \leq \lambda_I < 1$ as hot-spots cook-off within the microstructure. It is further assumed that the induction period is energetically inconsequential at the macro-scale. This term assumes that vigorous combustion progresses at a rate determined by the gas pressure at the instant of ignition; consequently, this model can give predictions that differ from reactive burn models that impose a constant ignition pressure. Different modes of transition to detonation are not expected to be accurately described by Eq. (13) due to the simplistic nature of the pressure-dependent burn law. This simple model is chosen as a first attempt to better understand how the ignition period can influence detonation transition over a wide range of pressure.

Figure 21 summarizes predictions for the variation in time t^* and distance x^* to detonation break-out within the material following impact with input shock pressure for porous HMX having $\bar{\phi}_0 = 0.68$ and 0.84 ; these plots are commonly referred to as Pop-plots. Also shown in the figure are initiation time and run distance data reported in the literature for porous HMX having $\bar{\phi}_0 = 0.65$ [7, 8, 10, 12] and $\bar{\phi}_0 = 0.86$ [8]. Though these materials have similar packing densities, the particle size distributions differ; therefore, these results are only intended to illustrate the leading-order effects of packing density on ignition and initiation. As seen in Fig. 21(a), the initiation time for each material (dotted curve) is largely controlled by ignition for strength dominated shocks, where ignition time curves are plotted as solid lines; such processes are therefore ignition controlled. These ignition curves are slightly offset from those predicted by the continuum theory at higher pressure (dashed lines) due to the influence of shock rise time in the implementation of Eq. (12). As input pressure increases, predicted initiation times are long compared to ignition times and are controlled by the growth of reaction to detonation; such processes are growth controlled. Predicted initiation times for $\bar{\phi}_0 = 0.68$ compare favorably to those measured by Dick[7] for high pressure shocks. The shock pressure required for transition from ignition to growth controlled initiation increases with packing density, and is estimated to be approximately 0.2 GPa for $\bar{\phi}_0 = 0.68$ and 0.4 GPa for $\bar{\phi}_0 = 0.84$.

Figure 21(b) summarizes the corresponding predicted variation in run distance to detonation. A couple observations are noteworthy. First, due to a complex transition mode, ignition controlled initiation is characterized by run distances associated with the evolution of detonation

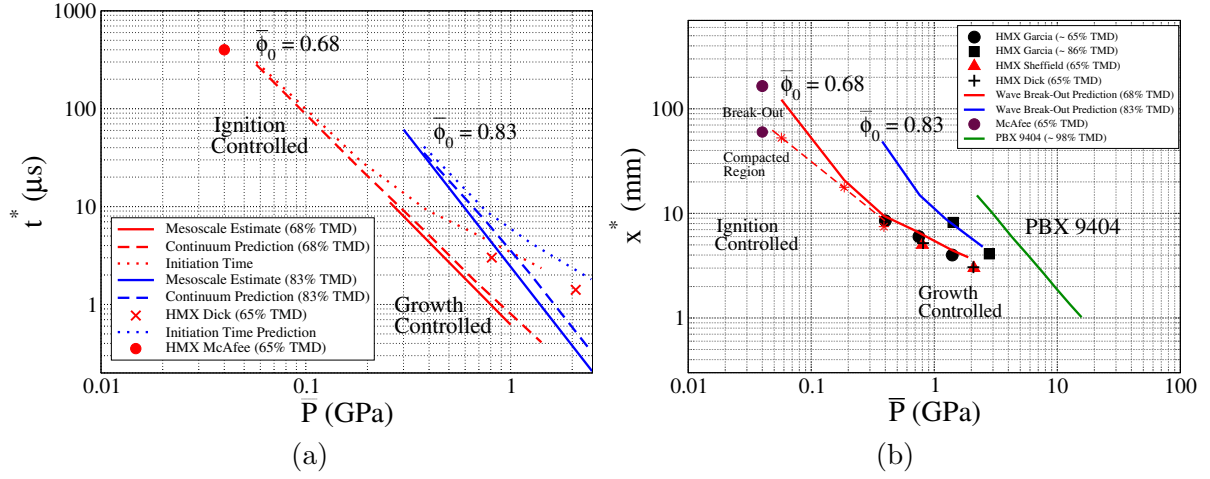


Figure 21: Plots showing the (a) ignition and initiation times, and (b) initiation distances for $\phi_0 = 0.68$ and $\phi_0 = 0.83$.

in compacted material behind the lead shock and the break-out of detonation into ambient material. These distances merge with increasing shock pressure as the initiation process becomes growth controlled. Second, slopes of the initiation curves (given by $\partial \log x^* / \partial \log \bar{P}$) slightly decrease with increasing shock pressure for ignition controlled processes, but approach an approximately constant value for growth controlled processes that depends on ϕ_0 . Higher ϕ_0 results in a marginally higher slope, possibly due to the larger change in effective hot-spot formation rate with pressure. Also shown in Fig. 21(b) for perspective is the measured run distance to detonation for the plastic-bonded explosive PBX 9404 (98% TMD HMX). Relative to $\phi_0 = 0.84$, the run distance curve for this material has higher slope, suggesting a larger variation in hot-spot formation rate with pressure, and requires higher shock pressure for a given run distance; as such, it is considered less sensitive than low density HMX.

Though the reactive burn model formulated in this effort gives results that are commensurate with time and run distance data, not all details of the transition mechanism are accurately predicted following ignition due to the simple form of the pressure-dependent burn law used. This deficiency is particularly apparent for ignition controlled initiation that involves complex temporal and spatial interactions between compaction and combustion waves within material behind the lead shock.

5. **Computational analysis of weak initiation of low density HMX.** [Rao and Gonthier, 2015 B; Rao and Gonthier, 2016 A; Rao and Gonthier, 2016 B] Low pressure (weak) initiation of low density granular HMX occurs by a complex mechanism that leads to a prompt (or discontinuous) transition to detonation within the material due to compaction shock interactions. These interactions influence ignition, flame spread, and subsequent transition by affecting dissipative heating within the microstructure during pore collapse. Details of the transition mechanism depend on initial packing density and input shock strength. In this effort, computations were performed using a multiphase reactive flow model to examine how the transition mechanism varies with input shock strength for granular HMX (68% TMD). As mentioned, the burn model outlined in Item 4 of this section does not accu-

rately describe details of the transition mechanism due to the overly simplistic nature of the pressure-dependent burn law despite its accuracy in predicting Pop-plots. The improved model accounts for pressure-dependent ignition, and subsequent burn depends on the local dissipative work, porosity, and pressure. The dependence on dissipative work is motivated by mesoscale M&S that indicated a significant increase in hot-spot size and spatial proximity within the microstructure as shock induced dissipative work increases, suggesting an increase in flame spread rate. Predictions highlight the variation in transition mechanism with increasing input shock strength and identify conditions that favor the formation of retonation waves during transition.

The volumetric mass exchange term \mathcal{C}_s is again described by Eq. (13), where the subsequent burn associated with gas production and energy release is now given by

$$f = \begin{cases} \alpha_L \left(\frac{\phi_s}{d_0} \right) \sigma_{ref} \left(\frac{P_g}{P_{ref}} \right) & \text{for } \phi_s \leq \phi_{crit} \\ (\alpha_L + \alpha_H) \left(\frac{\phi_s}{d_0} \right) \sigma_{ref} \left(\frac{P_g}{P_{ref}} \right) & \text{for } \phi_s > \phi_{crit}. \end{cases} \quad (14)$$

Here, α represents a dimensionless volumetric burn surface area prefactor, d_0 is particle size, and σ_{ref} is a characteristic regression velocity corresponding to pressure P_{ref} . Generally, $\alpha = \alpha(\phi_s, w_d)$, where w_d is mass specific shock dissipative work that can account for desensitization. This burn rate reflects a transition from normal regressive burn, characterized by α_L , to hot-spot facilitated burn, characterized by α_H , for strong pressure dominated shocks that have $\phi_s \approx 1$ and high values of w_d . Hot-spot facilitated burn is associated with a significant increase in burn area due to the ubiquitous formation of hot-spots. The dependence on ϕ_{crit} is chosen because DDT tube tests [10] indicate a drop in burn rate for approximately $\phi_s > 0.95$ prior to the onset of a hot-spot facilitated burn-type mechanism. For $\phi_s \leq \phi_{crit}$, a constant prefactor α_L is used and the burn is solely dependent on gas pressure. The prefactor α_H is given by

$$\alpha_H = \alpha_{min} + (\alpha_{max} - \alpha_{min}) \left(1 + \exp \left(\frac{-(w_d - w_{ref})}{\Delta} \right) \right)^{-1}. \quad (15)$$

In this effort, the values are $d_0 = 100 \mu\text{m}$, $\sigma_{ref} = 10 \text{ m/s}$, $P_{ref} = 0.1 \text{ GPa}$, $\alpha_L = 0.001$, $\alpha_{min} = 0.001$, $\alpha_{max} = 0.2$, $w_{ref} = 20 \text{ kJ/kg}$, and $\Delta = 0.5 \text{ kJ/kg}$. Different detonation transition mechanisms can be described by Eq. (14) due its dependence on ϕ_s , P_g , and w_d . Though conceptually similar to other models [13, 14], this model incorporates microstructure-dependent hot-spot predictions obtained by meso-scale M&S and accounts for hot-spot facilitated burn in terms of compaction shock dissipation to better characterize desensitization by shock interaction effects.

Figure 22 illustrates a predicted transition mechanism in low density HMX having $\phi_0 = 0.68$ for an input shock corresponding to a piston speed of $U_P = 200 \text{ m/s}$. The input shock in this case is strength dominated and it triggers an ignition controlled initiation process. The steady primary (input) compaction shock, labeled **c₁**, eliminates most of the porosity as it propagates a relatively long distance into the ambient material prior to the onset of burn near the piston surface at approximately $t = 25 \mu\text{s}$ following impact. Subsequently, regressive burn near the piston drives the formation of a secondary compaction shock, labeled **c₂**, due to the low permeability of combustion gases into dense material precompact by the primary shock. The secondary shock eliminates residual porosity resulting in the formation

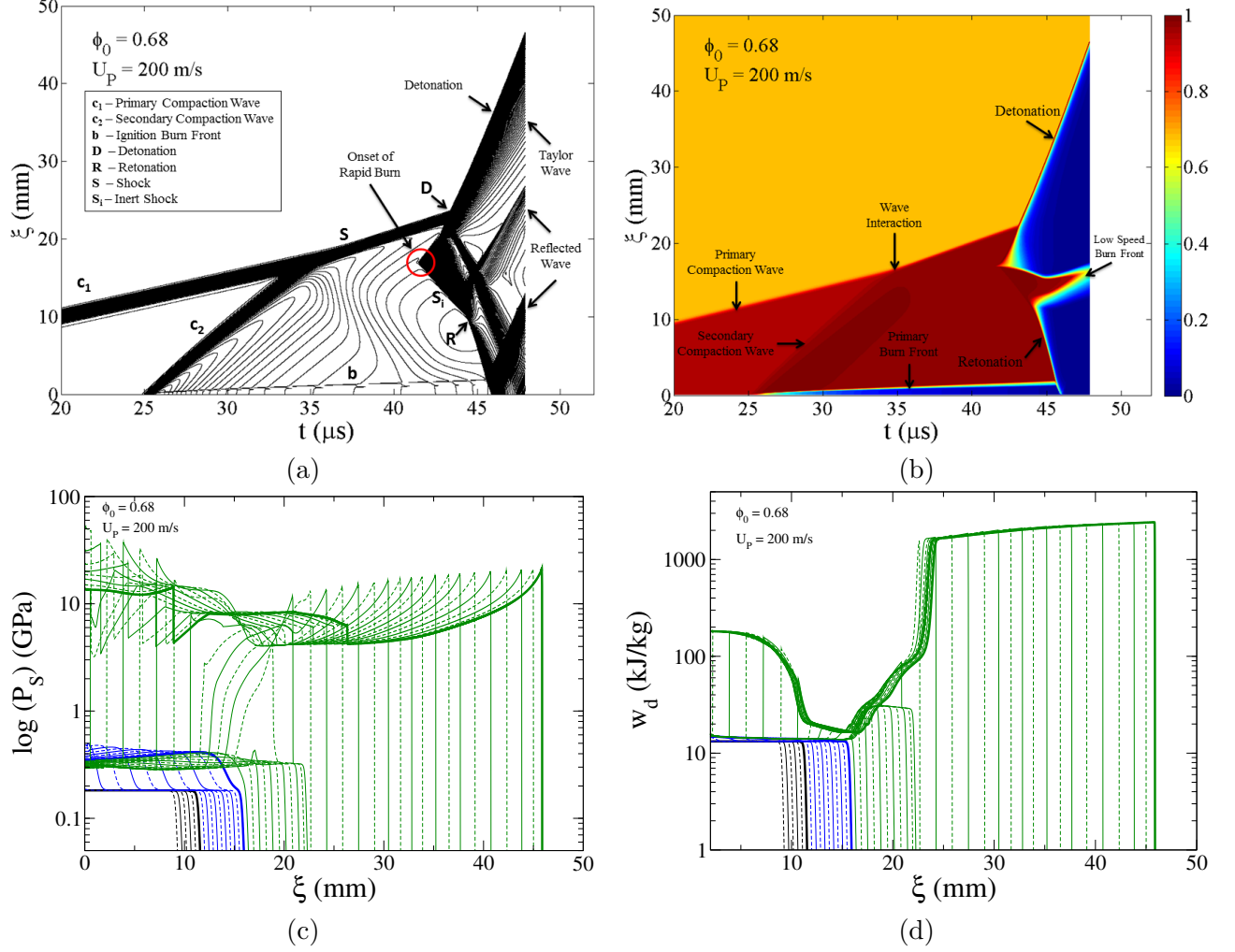


Figure 22: Predicted (a) bulk/mixture pressure contours showing compaction shock and ignition front trajectories in the characteristic plane; (b) solid/explosive volume fraction contours in the characteristic plane; (c) variation in bulk pressure with position at various times; and (d) variation in dissipative compaction work with position at various times. The material is low density HMX ($\phi_0 = 0.68$) and the input shock corresponds to a supporting piston speed of $U_P = 200$ m/s. Position is shown in a piston-attached reference frame.

of an inert solid “plug” that increases in width as it propagates forward [10]. This burn supported secondary shock causes less dissipation than those induced by weaker input shocks ($\approx U_p \leq 150$ m/s) because of slightly lower residual porosity behind the primary shock which is indicative of desensitization. The secondary shock overtakes the primary shock at approximately $t = 35 \mu\text{s}$ causing a significant increase in dissipation with a slight reduction in pressure. Consequently, the rapid onset of vigorous burn is predicted to occur within the compacted region at approximately $t = 43 \mu\text{s}$ after a short ignition delay following shock passage. At this location and time, $w_d \rightarrow w_{ref} = 20$ kJ/kg and α_H quickly increases resulting in hot-spot facilitated burn. This rapid onset of vigorous burn results in a “thermal-explosion-like” (or SDT-like) event which produces a forward propagating reactive shock and a backward propagating inert shock. The reactive shock quickly transitions to a Chapman-Jouguet (CJ) detonation, whereas the inert shock slowly increases in strength until it abruptly transitions into a strong reactive compression/retonation wave as $w_d \rightarrow w_{ref}$. These predictions indicate that the formation of retonation waves requires the occurrence of a SDT-like event which drives a backward propagating inert shock that becomes sufficiently strong to trigger hot-spot facilitated burn before interacting with the primary burn front.

Though not shown here, weaker input shocks, which also involve SDT-like events, do not result in retonation as the inert shock strength is insufficient to trigger hot-spot facilitated burn prior to interacting with the primary burn front. Stronger input shocks that are pressure dominated eliminate all porosity and result in a continuously accelerating combustion/detonation wave that forms within the compacted region whose pressure exceeds the Chapman-Jouguet value of the ambient material. In these cases, the transition mechanism is largely continuous, with ignition induction time comparable to that required for transition following ignition.

5 Personnel Supported

1. Keith A. Gonthier, Mechanical and Industrial Engineering Department, Louisiana State University (Associate Professor and PI).
2. John Gilbert, Mechanical and Industrial Engineering Department, Louisiana State University (Graduate Research Assistant). M.S. Thesis Title: Characterizing Impact Induced Hot-Spot Morphology in Granular Solid Explosive. **Graduated—2012**
3. Michael W. Crochet, Mechanical and Industrial Engineering Department, Louisiana State University (Graduate Research Assistant). Ph.D. Thesis Title: Modelling, Numerical Analysis, and Predictions for the Detonation of Multi-Component Energetic Solids. **Graduated—2013**
4. Sunada Chakravarthy, Mechanical and Industrial Engineering Department, Louisiana State University (Graduate Research Assistant). Ph.D. Thesis Title: Meso-Scale Analysis of Deformation Induced Heating in Granular Metalized Explosives by Piston Supported Waves. **Graduated—2014**
5. Pratap Rao, Mechanical and Industrial Engineering Department, Louisiana State University (Graduate Research Assistant). Ph.D. Candidate. Ph.D. Thesis Topic: Mesostructure-Dependent Ignition and Burn Modeling of Low Density Explosive. **Anticipated Graduation Date—August 2016**

6 Publications and Conference Presentations

1. Chakravarthy, S., Gonthier, K. A., and Rumchik, C. G., 2010, “Mesoscale Analysis of Deformation Wave Heating in Metalized Solid Explosive,” presented at the 2010 Conference on New Models and Hydrocodes for Shock Wave Processes in Condensed Matter, May 24-28, Paris, France. EPJ Web of Conferences, Vol. 10, 00010 (2010). DOI: 10.105/epjconf/20101000010. [**Chakravarthy, et al., 2010**]
2. Chakravarthy, S., and Gonthier, K. A., 2010, “Formulation of Macroscale Compaction Dynamics based on Mesoscale Simulations of Uniaxial Waves in Granular Explosive,” presented at the 2010 Southeastern Section Meeting, American Physical Society, October 20-23, Louisiana State University, Baton Rouge, Louisiana. [**Chakravarthy and Gonthier, 2010**]
3. Gonthier, K. A., 2010, “Mesomechanics of Deformation Wave Heating in Granular Explosive,” presented at The Shock and High Strain Rate Properties of Matter, September 7-10, Cavendish Laboratory, Cambridge University, Cambridge, United Kingdom. [**Gonthier, 2010**]
4. Chakravarthy, S., and Gonthier, K. A., 2011, “Mesoscale Analysis of Deformation Wave Structure and Dissipation in Metalized Solid Explosive,” presented at the 17th Biennial International Conference of the APS Topical Group on Shock Compression of Condensed Matter, June 26-July 1, 2011, Chicago, Illinois. (Abstract published in the Bulletin of the American Physical Society, Series II, Vol. 56, No. 6, June 2011; ISSN 0003-0503.) **Chakravarthy and Gonthier, 2011**]
5. Crochet, M. W., Gonthier, K. A., and Tohline, J. E., “A Modified Central Finite-Volume Scheme for Hyperbolic Systems with Nozzling Sources,” presented at the 42nd AIAA Fluid Dynamics Conference and Exhibit, New Orleans, LA, June 25-28, 2012. **Crochet, et al., 2012**]
6. Gilbert, J., *Characterizing Impact Induced Hot-Spot Morphology in Granular Solid Explosive*, M.S. Thesis, Louisiana State University, Baton Rouge, Louisiana, 2012. (Available at: <http://etd.lsu.edu/docs/available/etd-10082012-132131/>) [**Gilbert, 2012**]
7. Gilbert, J. N., and Gonthier, K. A., 2012, “Meso-Scale Computations of Uniaxial Waves in Granular Explosives—Analysis of Deformation Induced Ignition,” AIAA-2012-0433, presented at the 50th AIAA Aerospace Sciences Meeting, January 9-12, 2012, Nashville, Tennessee. [**Gilbert and Gonthier, 2012**]
8. Chakravarthy, S., Gonthier, K. A., and Panchadhara, R., 2013, “Analysis of Meso-Scale Heating by Piston Supported Waves in Granular Metalized Explosive,” *Modeling and Simulation in Materials Science and Engineering*, 21, doi:10.1088/0965-0393/21/5/055016. [**Chakravarthy, et al., 2013 A**]
9. Chakravarthy, S., and Gonthier, K. A., 2013, “Dissipative Heating in Porous Solid Explosives: Correlation of Thermomechanical Fluctuations and Microstructure,” presented at the Eighteenth Biennial International Conference of the APS Topical Group on Shock Compression of Condensed Matter (APS-SCCM), July 7-12, 2013, Seattle, Washington. (Abstract published in the Bulletin of the American Physical Society, Vol. 58, No. 7, July 2013.) [**Chakravarthy, et al., 2013 B**]

10. Crochet, M. W., *Modelling, numerical analysis, and predictions for the detonation of multi-component energetic solids*, Ph.D. Thesis, Louisiana State University, Baton Rouge, Louisiana, 2013. (Available at <http://etd.lsu.edu/docs/available/etd-11112013-154655/>) [**Crochet, 2013**]
11. Gilbert, J. N., Chakravarthy, S., and Gonthier, K. A., 2013, "Computational Analysis of Hot-Spot Formation by Quasi-Steady Deformation Waves in Porous Explosive," *Journal of Applied Physics*, 113, pp. 194901-19. [**Gilbert, et al., 2013**]
12. Rao, P., Chakravarthy, S., and Gonthier, K. A., 2013, "Computational Analysis of Compaction Wave Dissipation in Porous Solid Explosives," AIAA-2013-0819, presented at the 51st AIAA Aerospace Sciences Meeting, January 7-10, 2013, Grapevine, Texas. [**Rao, et al., 2013**]
13. Chakravarthy, S. *Meso-Scale Analysis of Deformation Induced Heating in Granular Metalized Explosives by Piston Supported Waves*, Ph.D. Thesis, Louisiana State University, Baton Rouge, Louisiana, 2014. (Available at: <http://etd.lsu.edu/docs/available/etd-08102014-085202/>) [**Chakravarthy, 2014**]
14. Gonthier, K. A., and Chakravarthy, S., "Shock Induced Ignition of Porous HMX—Computational Examination of Hot-Spot Formation Rates," Proceedings of the 15th International Detonation Symposium, San Francisco, California, July 13-18, 2014, pp. 1285-1294. (Office of Naval Research publication number 43-280-15.) [**Gonthier and Chakravarthy, 2014**]
15. Rao, P., and Gonthier, K. A., 2014 "Analysis of Compaction Wave Dissipation in Porous Metalized Explosive," *Journal of Physics: Conference Series*, 500 (2014), 152006, doi:10.1088/1742-6596/500/15/152006. (Presented at the Eighteenth Biennial International Conference of the APS Topical Group on Shock Compression of Condensed Matter (APS-SCCM), Seattle, Washington, July 7-12, 2013.) [**Rao and Gonthier, 2014 A**]
16. Rao, P., and Gonthier, K. A., "Reactive Burn Modeling of Porous Solid Explosives," AIAA-2014-3810, presented at the AIAA Propulsion and Energy Forum and Exposition (AIAA Propulsion and Energy 2014), Cleveland, Ohio, July 28-30, 2014. [**Rao and Gonthier, 2014 B**]
17. Crochet, M. W., and Gonthier, K. A., 2015, "A Multi-Phase Theory for the Detonation of Granular Explosives Containing an Arbitrary Number of Solid Components," *International Journal of Multiphase Flow*, 77, pp. 76-89. [**Crochet and Gonthier, 2015**]
18. Rao, P., and Gonthier, K. A., "Analysis of Dissipation Induced by Successive Planar Shock Loading of Granular Explosive," AIAA-2015-3708, presented at the 2015 AIAA Propulsion and Energy Forum and Exposition, Orlando, Florida, July 27-29, 2015. Recipient of the 2015 Arthur D. Rhea Award for the Best Paper presented on Energetic Components and Systems. [**Rao and Gonthier, 2015 A**]
19. Rao, P., and Gonthier, K. A., "Analysis of Compaction Shock Interactions During DDT of Low Density HMX," presented at the 19th Biennial APS Conference on Shock Compression of Condensed Matter, Tampa, Florida, June 14-19, 2015. (In Press) [**Rao and Gonthier, 2015 B**]

7 Workshop and Meeting Presentations

1. Gonthier, K. A., October 25-27, 2011, “Probabilistic Ignition Modeling of Energetic Solids,” AFRL Hugh James Workshop, University of Florida REEF Facilities, Shalimar, Florida.
2. Gonthier, K. A., February 8-10, 2012, “Modeling Multi-Scale Wave Dissipation in Reactive Solid Composites,” presented at the 2nd Structural Nano-Energetics (SNE) Project Agreement Meeting between The Singapore Ministry of Defence and the U.S. Department of Defense, Energetics Research Institute (EnRI), Singapore.
3. Gonthier, K. A., May 24, 2012, “Meso-Mechanics of Shock Loaded Granular Solids,” presented at the NASA Jet Propulsion Laboratory, Pasadena, California, May 24, 2012.
4. Gonthier, K. A., September 17-19, 2012, “Modeling Multi-Scale Wave Dissipation in Reactive Solid Composites—*A Statistical Analysis of Hot-Spots*,” presented at the 3rd Structural Nano-Energetics (SNE) Project Agreement Meeting between The Singapore Ministry of Defence and the U.S. Department of Defense, U.S. Army Research and Development Engineering Center, Picatinny Arsenal, New Jersey.
5. Gonthier, K. A., May 26-28, 2014, “Deformation Induced Ignition of Porous Energetic Materials—*Accounting for Microstructure*,” presented at the Synthesis, Formulation, and Characterization of Structural Nano-Energetics (SNE) Project Review, Project Agreement Meeting between The Singapore Ministry of Defence and the U.S. Department of Defense, Energetics Research Institute (EnRI), Singapore.
6. Gonthier, K. A., July 13-15, 2015, “Initiation of Low Density Granular Energetic Materials—Current Developments and Collaborative Opportunities with LSU,” presented at the Synthesis, Formulation, & Characterization of Structural Nano Energetics (SNE) Project Agreement Meeting, Air Force Research Laboratory, Eglin AFB, Florida.

8 Manuscripts in Review/Preparation

- Chakravarthy, S., and Gonthier, K. A., “Effects of Mesostructure on Shock Induced Heating of Granular Metalized Explosive,” *Journal of Applied Physics*, in review. [**Chakravarthy and Gonthier, 2016**]
- Rao, P., Gonthier, K. A., and Chakravarthy, S., “Compaction Shock Dissipation in Granular Explosive,” in preparation.

9 Abstracts Accepted for Presentation

- Rao, P., and Gonthier, K. A., “The Evolution of Retonation During DDT of Low Density HMX,” abstract accepted for presentation at the AIAA Propulsion and Energy Forum and Exposition (Propulsion and Energy 2016), Salt Lake City, Utah, July 25-27, 2016. [**Rao and Gonthier, 2016 A**]
- Rao, P., and Gonthier, K. A., “A Microstructure-Based Reactive Flow Model for Shock Initiation of Low Density Granular Explosives,” abstract accepted for presentation at the ICMF 2016 International Conference on Multiphase Flow Firenze, Italy, May 22-27, 2016. [**Rao and Gonthier, 2016 B**]

References

- [1] Barua, A., and Zhou, M., “A Lagrangian Framework for Analyzing Microstructural Level Response of Polymer Bonded Explosives,” *Modelling Simul. Mater. Sci. Eng*, 19, 2011, pp. 005001-005025.
- [2] Baer, M. R., and Nunziato, J. W., “A Two-Phase Mixture Theory for the Deflagration-to-Detonation Transition in Reactive Granular Materials,” *International Journal of Multiphase Flow*, Vol. 12, 1986, pp. 861-889.
- [3] Baer, M. R., “Modeling Heterogeneous Materials at the Mesoscale,” *Thermo. Acta*, 384, 352, 2002.
- [4] Bdzil, J. B., Menikoff, R., Son, S. F., Kapila, A. K., and Stewart, D. S., 1999, “Two-Phase Modeling of Deflagration-to-Detonation Transition in Granular Materials: A Critical Examination of Modeling Issues,” *Physics of Fluids*, Vol. 11, No. 2, 378.
- [5] Crochet, M. W., *Modelling, numerical analysis, and predictions for the detonation of multi-component energetic solids*, Ph.D. Thesis, Louisiana State University, 2013. (Available at <http://etd.lsu.edu/docs/available/etd-11112013-154655/>)
- [6] Crochet, M. W., and Gonthier, K. A., “A Multi-Phase Theory for the Detonation of Granular Explosives Containing an Arbitrary Number of Solid Components,” *J Comp Phys*, Vol. 255, pp. 266292, 2013.
- [7] Dick, J. J., “Measurement of the Shock Initiation Sensitivity of Low Density HMX” *Combustion and Flame*, Vol. 54, pp. 121-129, 1983.
- [8] Garcia, F., Vandersall, K. S., and Tarver, C. M., “Shock Initiation Experiments with Ignition and Growth Modeling on Low Density HMX” *Journal of Physics: Conference Series*, Vol. 500, No. 052048, 2014. (doi:10.1088/1742-6596/500/052048. Presented at the 18th Biennial International Conference of the APS Topical Group on Shock Compression of Condensed Matter, July 7-12, 2013, Seattle, Washington.)
- [9] Marsh, S. P., *LASL Shock Hugoniot Data*, University of California Press, Berkeley, CA, 1980.
- [10] McAfee, J. M., Asay, B. W., Campbell, W., and Ramsay, J. B., Deflagration to Detonation Transition in Granular HMX, *Proceedings of the Ninth (International) Detonation Symposium*, 1989, pp. 265-278.
- [11] Panchadhar, R., and Gonthier, K. A., “Mesoscale Analysis of Volumetric and Surface Dissipation in Granular Explosive Induced by Uniaxial Deformation Waves,” *Shock Waves*, 21(1), pp. 43-61, (2011).
- [12] Sheffield, S. A., Gustavsen, R. L., and Anderson, M. U., 1997, “Shock Loading of Porous High Explosives,” *High-Pressure Shock Compression of Solids IV*, Springer-Verlag New York, Inc., New York, 24.
- [13] Son, S. F., Asay, B. W., and Bdzil, J. B., “Inert plug formation in the DDT of granular energetic materials,” *Proceedings of the conference of the American Physical Society topical group on shock compression of condensed matter*, Vol. 370, No. 1, AIP Publishing, 1996.

- [14] Xu, S., and Stewart, D. S., “Deflagration-to-Detonation Transition in Porous Energetic Materials: A Comparative Model Study,” *J Eng Math*, Vol. 31, pp. 143-172, 1997.
- [15] Lee, E. L., and Tarver, C. M., “Phenomenological Model of Shock Initiation in Heterogeneous Explosives,” *Phys Fluids*, Vol. 23, pp. 2362-2372, 1980.
- [16] Torquato, S., “Random Heterogeneous Materials: Microstructure and Macroscopic Properties”, Springer, 1st edition, New York, (2002).

DISTRIBUTION LIST
DTRA-TR-16-77

DEPARTMENT OF DEFENSE

DEFENSE THREAT REDUCTION
AGENCY
8725 JOHN J. KINGMAN ROAD
STOP 6201
FORT BELVOIR, VA 22060
ATTN: A. DALTON

DEFENSE TECHNICAL
INFORMATION CENTER
8725 JOHN J. KINGMAN ROAD,
SUITE 0944
FT. BELVOIR, VA 22060-6201
ATTN: DTIC/OCA

**DEPARTMENT OF DEFENSE
CONTRACTORS**

QUANTERION SOLUTIONS, INC.
1680 TEXAS STREET, SE
KIRTLAND AFB, NM 87117-5669
ATTN: DTRIAC